CFD STUDY OF NATURAL CONVECTION HEAT TRANSFER OF AN ROC-BASED THERMAL ENERGY STORAGE SYSTEM

A Thesis

Presented to the

Faculty of

California State Polytechnic University, Pomona

In Partial Fulfilment

Of the requirements for the Degree

Master of Science

In

Mechanical Engineering

By

Justin Andrew Lee

2021

SIGNATURE PAGE

THESIS:	CFD STUDY OF NATURAL CONVECTION HEAT TRANSFER OF AN ROC-BASED THERMAL ENERGY STORAGE SYSTEM
AUTHOR:	Justin Andrew Lee
DATE SUBMITTED:	Summer 2021
	Department of Mechanical Engineering

Dr. Reza Baghaei Lakeh
Thesis Committee Chair
Mechanical Engineering _____

Dr. Kevin R. Anderson
Mechanical Engineering _____

Dr. Henry Xue
Mechanical Engineering _____

ACKNOWLEDGEMENTS

I would like to thank Professor Reza Baghaei Lakeh for welcoming me to his research project and always supporting my academic endeavors. He has been a great instructor and advisor to me, and especially during the COVID-19 lockdowns he has been supportive and given me and my team the motivation to achieve our research goals. I will forever be grateful for the advice and guidance through my research and that his instructions have made me a better writer and presenter.

I would also like to thank another individual instructor, Professor Kevin R. Anderson. I have learned so many advanced topics in your thermal fluids emphasis courses and I can't thank you enough for bringing advanced topics down to my level of understanding. Thank you for all of your help in class and revealing to me how capable I am. I thank the aforementioned two professors and staff in the Mechanical Engineering department for everything each of you have done to make my experience at Cal Poly Pomona the best I could have imagined.

To my research mates I thank you all for being supportive and cooperative with my research objectives. I relied on you when at times I felt I was coming up short and I am thankful we can still work effectively as a team, even via remote communication. We really hit it off this year and I only wish I could have had more time to interact with you all.

Lastly, to my family and significant other, I love you all and thank you for supporting me through my graduate school journey. Thank you for being patient with me and encouraging me along my path at obtaining a master's degree.

ABSTRACT

This thesis investigates the heat transfer mechanisms, through computational fluid dynamics (CFD), of a thermal energy storage (TES) device using the dehydrated reverse osmosis concentrate (ROC) as a phase change material (PCM). Inorganic salts (e.g., chloride salts) have gained attention in the energy field as an option for TES medium. Inorganic salts have the advantage of having high heat capacity, high melting temperature, and low cost that make them suitable for utility-scale thermal storage applications. The higher melting temperature could lead to higher efficiency in power generation.

The potential to use ROC, which is a byproduct of water desalination, has the potential to supply TES devices with an abundant PCM and it could solve some of the issues related to hazardous waste disposal at inland based water desalination plants. Prevention of release of this salty byproduct benefits the environment and at the same time its use as a TES helps conserve excess generated renewable energy during unfavorable weather conditions.

A computational model is developed on a commercial CFD software, ANSYS Fluent, and the results are verified and validated. The model aims to simulate the phase change process and buoyancy-driven flow in a square ROC-filled TES element. The computational results provide a predictive model for charge and discharge cycles, and can be used for further product development.

TABLE OF CONTENTS

LIST OF TABLES

LIST OF FIGURES

NOMENCLATURE

A_s	Surface Area, (m^2)
A_{mush}	Mushy Zone Constant, ($kg/sec*m^3$)
c_p	Specific Heat, (J/kg-K)
g	Gravity, (m/s^2)
E	Energy, (J)
H	Enthalpy, (J)
ΔH	Latent heat, (J)
h	Sensible Enthalpy, (J)
h_c	Convective Heat Transfer Coefficient, ($W/m^{2-}K$)
L	Latent heat of material, (J)
k	Thermal Conductivity, (W/m-K)
T	Temperature, (°C)
T_i	Initial temperature, (°C)
T_L	Liquidus Temperature, (°C)
T_S	Solidus Temperature, (°C)
T_W	Wall Temperature, (°C)
T_∞	Bulk Fluid Temperature, (°C)
T*	Dimensionless temperature
V_c	Control Volume, (m^3)

Greek Symbols

β	Liquid fraction
ε	Small number, 0.001, to prevent division by 0
μ	Viscosity (kg/m-sec)
υ	Velocity (m/sec)
ρ	Density (kg/m^3)

CHAPTER 1 INTRODUCTION

1.1 Desalination Waste Byproduct Issue

The increasing population in high density cities has caused an increase demand for potable water to an amount that cannot be replenished by natural sources such as rivers and ground water wells [1]. The alternative to piping water from further bodies of water is to build a desalination plant near those cities, especially since large cities tend to be built near large bodies of water; fresh or non-fresh. One widely adopted method of desalination is reverse osmosis (RO). To explain reverse osmosis the forward process is simply called osmosis, which is the spontaneous transport of water through a semipermeable membrane to equalize the solute concentration between both sides of the membrane. The osmosis phenomena are associated with added pressure against the membrane called osmotic pressure. The RO technology operates on the principle of going against the osmotic pressure in order for the water to be removed from the salty water. Desalination by reverse osmosis is an effective method for continuously producing fresh water from non-fresh water sources such as oceans and brackish water from lakes and streams. The byproduct of desalination is a concentrated brine that cannot efficiently be further filtered by reverse osmosis. Therefore, that brine, or reverse osmosis concentrate (ROC) must be disposed after the filtration process. The RO facilities that operate near oceans are allowed to dispose the ROC into the ocean as long as that stream of ROC is first diluted with more sea water and away from high populations of marine wildlife. The release of more concentrated salt water back into the oceans has devastating ecological

impact on the marine life in shallower coastal reefs [2]. Therefore, the ROC has to be sent farther into the ocean and away from known populated marine environments.

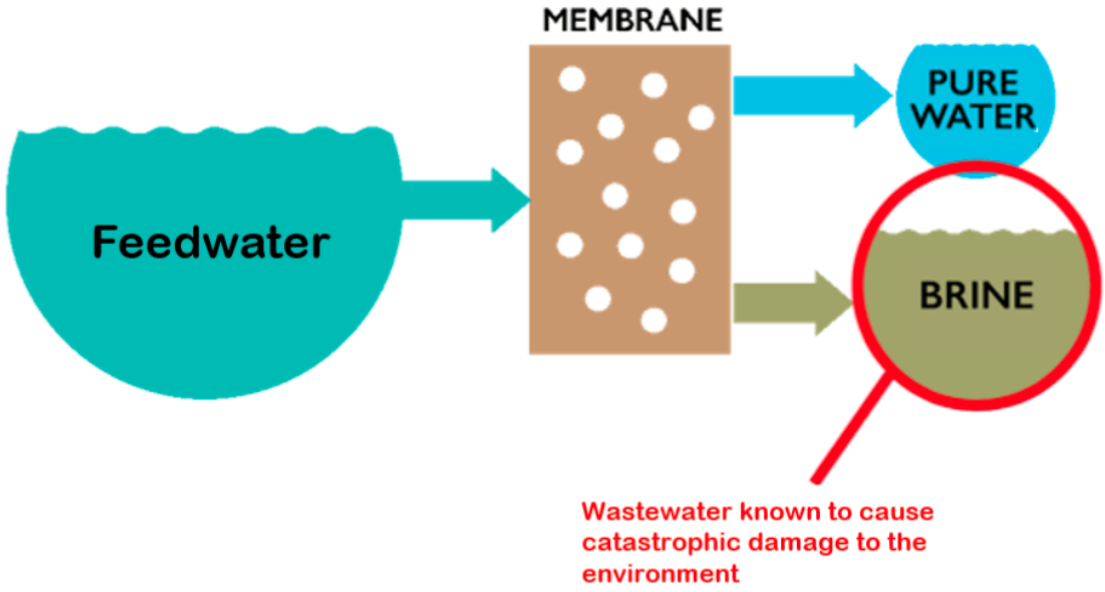

Figure 1-1. Illustrating where brine comes from and its environmental effects.

The inland RO facilities do not have oceans to discharge ROC and must develop alternative methods for disposing the salt and while generating fresh water. The inland facilities' only option is to use evaporation ponds, but this leads to accumulation of solid salt. An additional concern with evaporation ponds is the tendency to attract migrating birds that will mistakenly use ponds as resting stops and can suffer from ingestion of salty water. The dried solid salt can accumulate in several thousands of pounds of salt, and it is not economically feasible to separate pure salt compounds from the mixture. There is no current industrial adoption of ROC on the scale that can offset the accumulation of it through desalination. With no other method of ROC disposal other than to transport it away the inland RO facilities must face with the consequences of

storing all that salt. One idea to mitigate storage issues is to use the ROC as a TES medium, which will be discussed later in the TES part of this introduction.

1.2 Renewable Energy Issue

The increased addition of renewable energy sources such as solar and wind will offset the carbon emissions as demand for energy continues to grow [3]. During sunny weather the solar energy provides affordable energy to the grid and likewise windy days provide wind energy to the grid. While two renewable energy sources greatly benefit the reduction of the carbon footprint of energy consumption, both are what is known as intermittent energy sources. The intermittency means that solar and wind power production is determined by the weather, therefore the output is neither constant nor reliable. There are many technologies that are being developed to address the intermittency issues by means of energy storage and discharge methods. Battery energy storage systems (BESS) for storing excess renewable energy on the electric grid and its effectiveness is answered in a study by National Renewable Energy Laboratory (NREL) [3]. However, the high cost of batteries prohibits widespread adoption and competes with other mobile technologies that rely on battery technology. Kinetic energy storage has also been explored, but the material costs alone make it expensive since there needs to be more mass of material in order to store more energy. One promising energy storage technology is thermal energy storage (TES), specifically, with phase change material (PCM) as the energy storage medium.

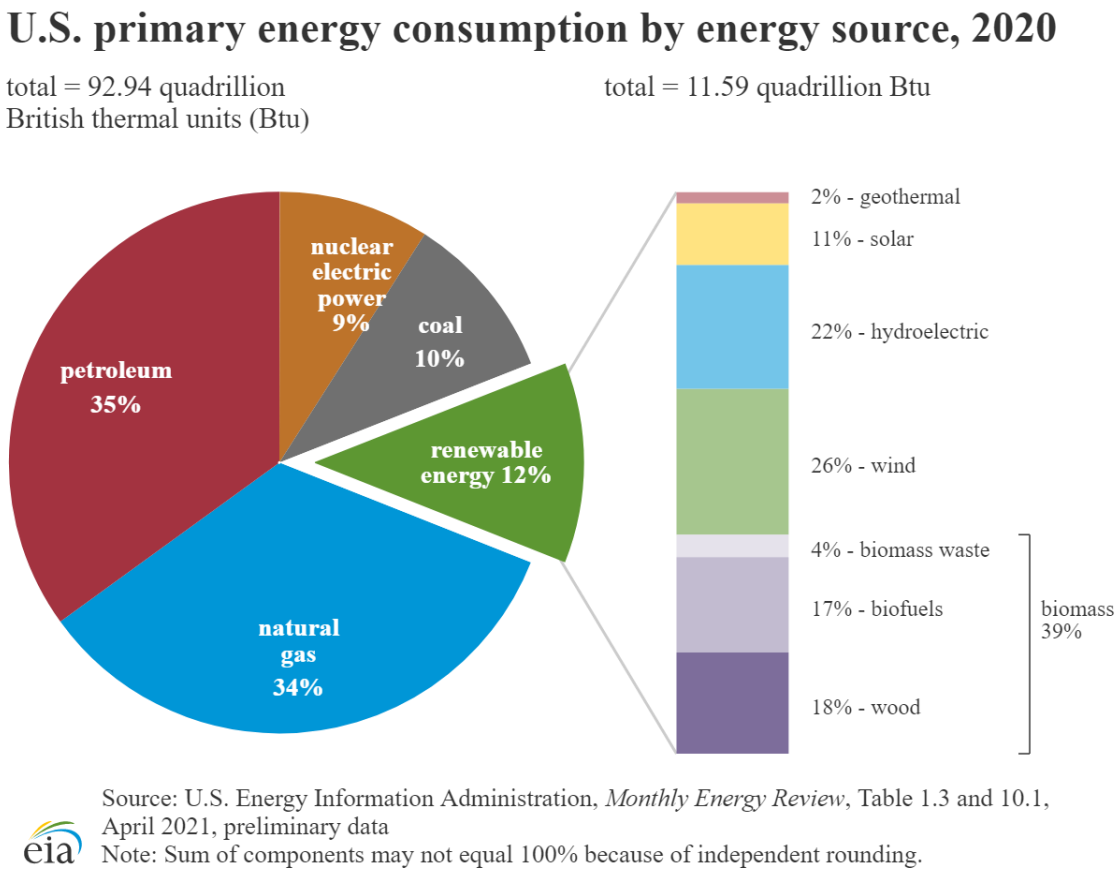

Figure 1-2. DOE pie chart of energy consumption by different sources.

While discussing the renewable energy issue, a further look that compares a U.S. average consumption of energy by category in Figure 1-2 and then a daily consumption and production of renewable energy in Figure 1-3. The pie chart of Figure 1-2 shows that the adoption of solar is just 11% of the renewable energy consumed which accounted for just 12% of overall consumption. That means solar energy only made up 1.32% of total energy consumed in the U.S. However, when solar is a dominant supplier of energy, like in the state of California, the production proportion has a stronger effect on the grid. The curve in Figure 1-3 is known as the 'Duck Curve', which is a representation of the difference in electricity demand and the amount of available solar energy throughout the

day [4]. There is an actual overproduction of energy from solar during the middle of the day and the grid companies must discharge the excess to prevent system overloading. The other issue presented in this graph is that energy demand ramps up in the afternoon when the sun is setting and not powering the solar energy systems. This is a problem that is appropriate for TES applications because the TES technology can convert directly heat from solar radiation into stored heat and then dispatch that energy when demand is high in the afternoon. The technology of TES is introduced in the next section to discuss how it is best implemented.

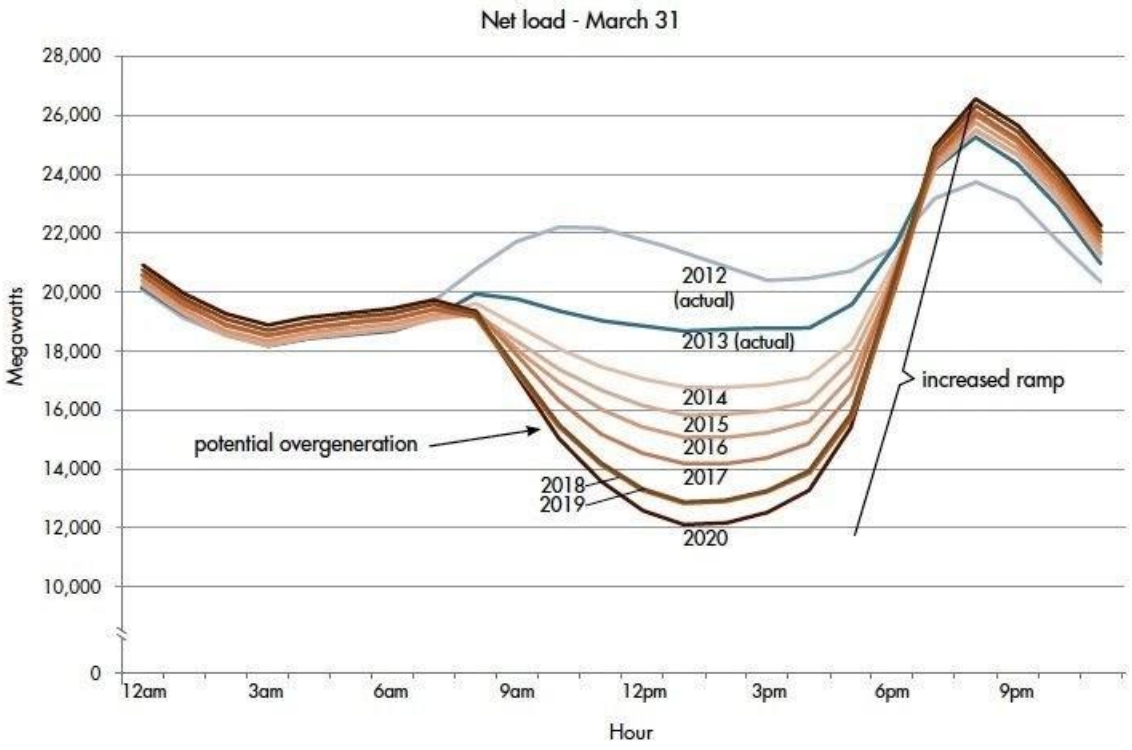

Figure 1-3. The 'duck curve' of electrical demand and production.

1.3 Thermal Energy Storage and Phase Change Materials

The principle behind TES is that a contained material is heated to a temperature that has enough useful energy to be extracted. The amount of energy that is stored can be in the form of sensible heat, which is heat stored through changes in its temperature or in the form of latent heat, which is heat stored during a phase change at a constant temperature. Latent heat is accomplished through the use of a PCM, which in practice changes phase between solid and liquid phase due to relatively similar density. The advantage of using PCMs in TES devices is there is a large quantity of latent heat that can be stored and the sensible heat in the liquid phase is usually greater than in the solid phase. The ability to change phase of a material makes it a more economical candidate for TES applications. Engineers have taken an interest in using salts as viable candidates of PCMs for their high melting temperature and low vapor pressure [5] [6]. Other inorganic salts have already been used as heat transfer fluids (HTFs) in advanced high-temperature concentrating solar power plants (CSP) [7] [8]. One widely adopted salt mixture is commercially marketed as Solar Salt, which is a 60/40 weight ratio of NaNO3 and KNO3 which melts at 220C and stored hot at 565C [9]. Other materials for TES applications could utilize chemical change without undergoing a physical phase change, but the scope of this research is focused on PCMs.

The engineering of a TES device by using a PCM would require knowledge of the thermophysical properties of melting point, density, specific heat capacity, thermal conductivity, and viscosity. PCMs made of pure substances have more predictable properties since most thermophysical properties are measured in their pure form. There is

a NIST database [10] of pure salt and some binary salt mixtures that have recorded thermophysical properties. Some properties are functions of temperature for specific temperature ranges and tolerances. The effort of using ROC as a PCM is much more difficult because the composition is made up of various minerals dissolved in the feed water which also differ by location. The hope is that there are common dominant components that have well-documented properties and that trace components do not significantly alter the bulk property.

The composition of sea water salt is well documented throughout many ocean chemistry measurements and consists primarily of NaCl salt. NaCl has much of its properties documented, even at melting temperatures. However, as mentioned earlier, seawater ROC is likely to be discharged back into the ocean instead of extracted as solid salt. The inland ROC contains more elements that lead to hard water such as calcium and magnesium. Together, the inland ROC is expected to contain any combination of chlorides, carbonates, and sulfates with the sodium, potassium, calcium and magnesium.

Overall, the complexity and untested properties of mixed salts such as that of inland ROC makes it more challenging to engineer it into a PCM for TES applications. To prevent analysis paralysis of understanding the ROC before designing a TES device, the assumption will be that the property of the ROC as a salt mixture will be the weighted average of the individual components. This weighted averaged thermophysical properties should be approximately close to the real property. Any such TES device that can handle a variety of ROC from different water sources should be built with a large operating range anyways, so therefore the exact thermophysical properties will be excused for sake of simulation development. The effort to address the issue of ROC disposal and TES

material selection and design is turned into the TESuROC project; short for Thermal Energy Storage using Reverse Osmosis Concentrate.

1.4 TES Device

The PCM used for TES would be best optimized for charging by melting during the day and discharging by solidification in the evening. There are two methods of charging the PCM, one by solar thermal and another by electric resistive heating. Solar thermal energy derived charging would be delivered through heat transfer fluid heating up from a solar field and then through the TES taking a path like a heat exchanger.

A TES device would have to be constructed in a way that the PCM is stationary and the heat delivered to the PCM resembles traditional heat exchanger design, such as shells, tubes, and fins. The discharge cycle should extract heat from the PCM at a rate suitable to power a Rankine cycle generator. Overall, a TES product using ROC as the PCM should be designed to be competitive in the energy market as a more affordable option for TES. The Sunshot Initiative is a U.S. Department of Energy program that sets out the goal that by 2030 the utility scale cost of energy should be $0.03 per kWh. By choosing to make a TES device using a processed byproduct the cost would go down and this makes ROC an attractive substitute for conventional PCMs.

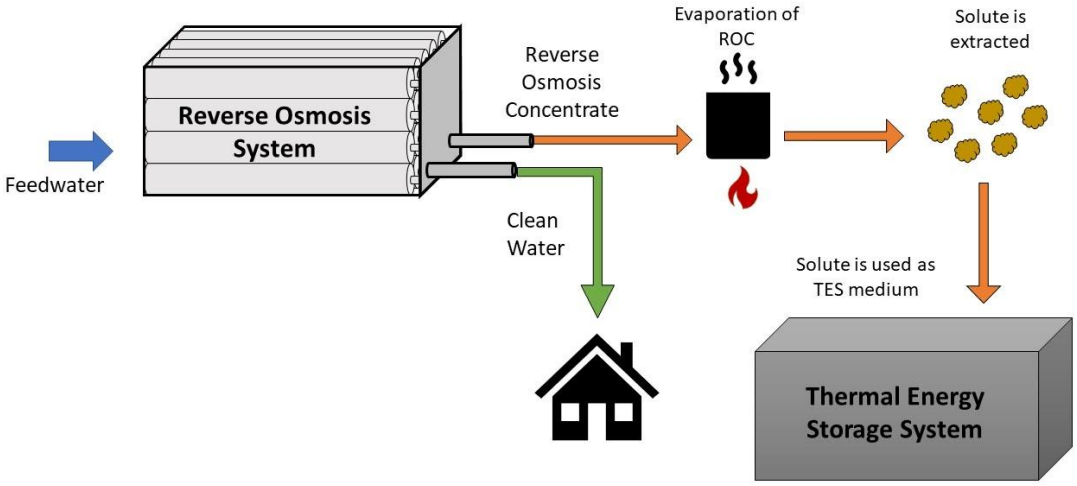

Figure 1-4. Process for extracting ROC into a TES device.

1.5 Scope of Research

The goal of the TESuROC project is to develop and integrate a working TES device that uses ROC as a PCM into a power generation system that stores solar thermal energy and excess grid energy. Figure 1-5 shows an illustration of analyzing the system from a broad and practical application to the smallest unit that can be analyzed under macroscopic transport phenomena effects. Figure 1-5 (a) is the 10,000 foot view of the research objectives. It is desirable to develop a system that has the power production of a contemporary power plant, complete with the unit operations of each component. Though this view has the greatest impact on influencing investors, it is insufficient at understanding the specific heat transfer mechanisms. To narrow the scope the TES unit is enlarged for more detail.

Working the way down to (b) of Figure 1-5 is a view of the TES unit, which has many features of a heat exchanger. It includes structures such as pipes, shells, tubes, and baffles. Heat exchanger analysis answers the overall heat transfer coefficient, and inlet and outlet temperatures. This topic is actually discussed in another TESuROC led study [11]. The goal of this thesis is to know how the heat transfer inside the salt element affects the overall performance of the TES unit, so the scope needs to be limited to just the ROC packed inside the tube.

Figure 1-5 (c) is the focus of this thesis. This is the deepest level for understanding macroscopic fluid and heat transfer mechanisms. At this level, the ROC is the only material present and is simulated under simple boundary and initial conditions. This level is also convenient for transforming the 3D to 2D perspective with the aid of axial symmetry. Information about the heat transfer performance of the ROC will inform how it will behave in a TES unit, and that unit design will inform how to build out a full system. Those details will not be discussed, but they are mentioned as a reminder of the goal of utility scale energy storage.

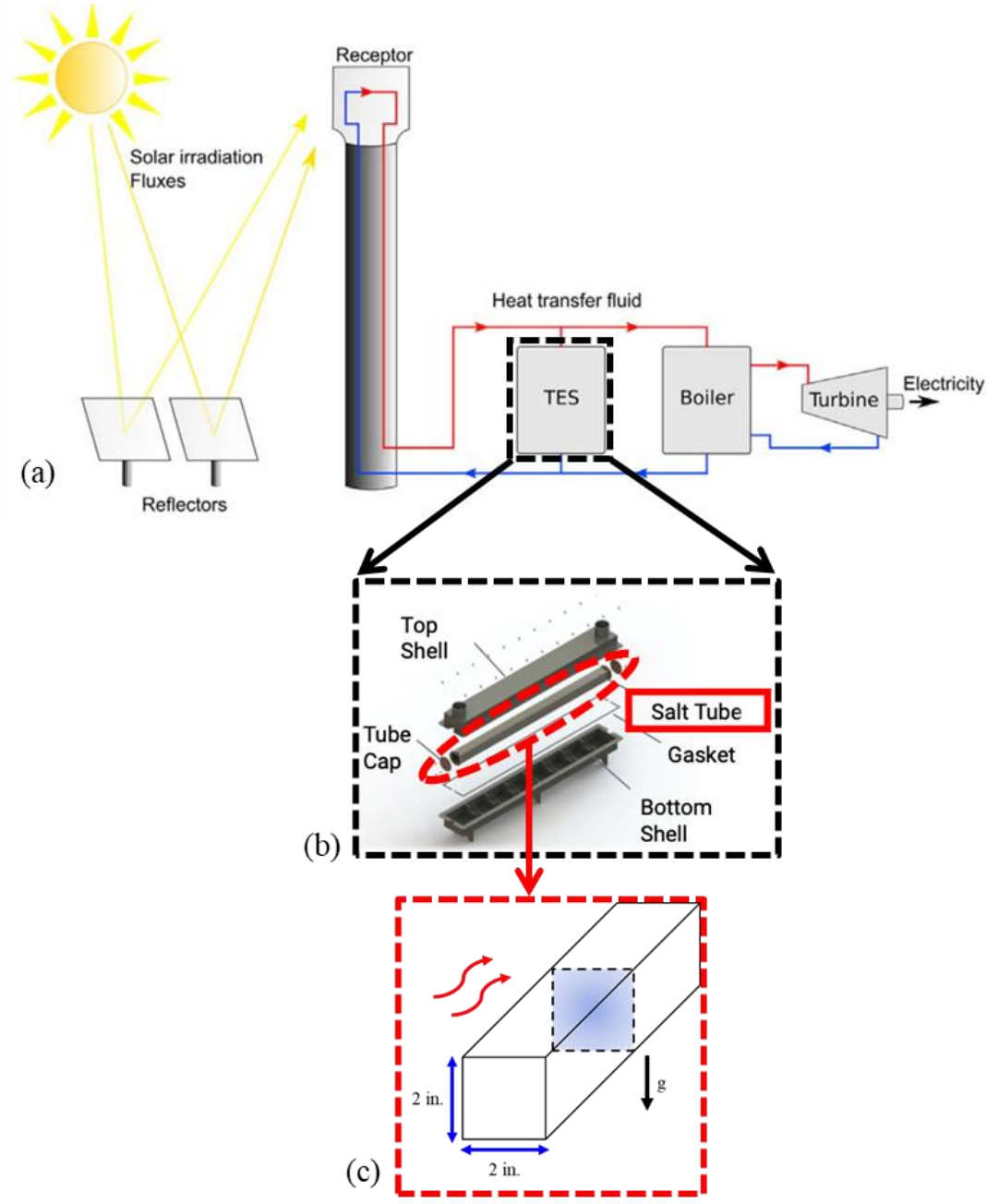

Figure 1-5. (a) Unit operations [12]. (b) TES unit. (c) 2D ROC container.

1.6 Modeling in CFD

Bringing together the thermophysical properties of the ROC and the existing TES device at Cal Poly Pomona allows for the simulation of the heat transfer occurring inside the PCM element. Since the ROC is expected to melt, there is a chance that the melting process will drive fluid flow by natural convection and therefore increase the rate of heat transfer. The aid of CFD software will greatly aid in the design of a TES device so that there is an understanding of the expected behavior inside the TES element. The objective of this CFD study is to quantify the phase of the PCM during charging and discharging, and determine how much convection and conduction each contributes to heat transfer. The CFD package, ANSYS Fluent, was used to simulate the governing equations that determines the heat transfer of the TES system. A simplified, fluid-domain only perspective is the scope of this study. A computational study that simultaneously calculates fluid flow in a heat exchanger, and solidification and melting would be too complicated and use up too much computational resources. This CFD study has already determined that convection contributes to the majority of heat transfer and that the operating conditions imposed on the salt element has the potential to be used in TES applications.

CHAPTER 2 METHODOLOGY

2.1 Geometry

The TESuROC project at Cal Poly Pomona has constructed a TES device that contains one PCM element in a square tube, with 2 inch sides and 40 inches long, that encases packed ROC. The cross section of the square tubing is modeled for CFD. The justification for simulating a 2D geometry that ignores end effects is that there is significantly less driving forces to cause flow in the axial direction. There is no pressure or buoyancy forces causing flow to cross into the z-direction, therefore the 2D simulation over a long tube is justified. Doing a 2D simulation versus 3D simulation saves computational time and represents symmetry along the cross sections of the tube.

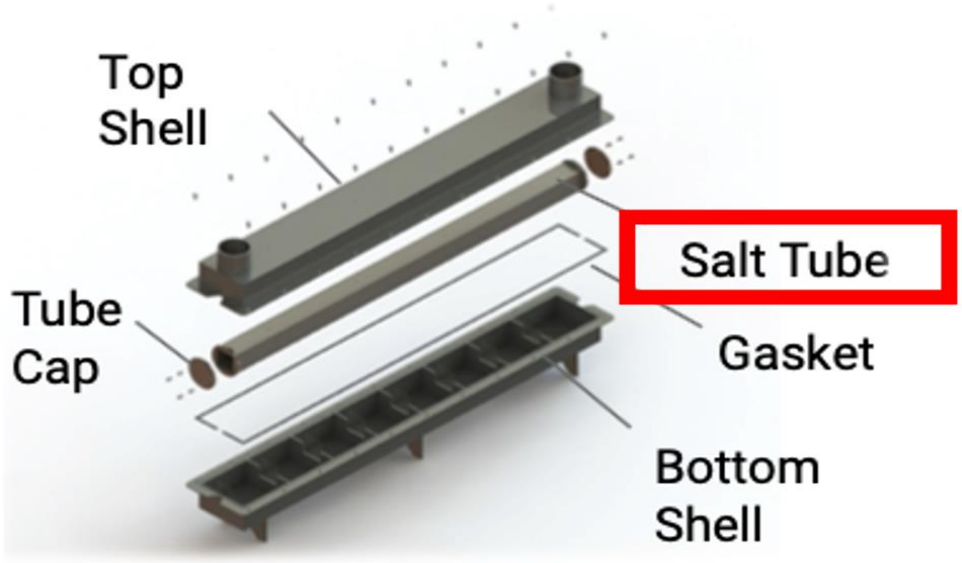

Figure 2-1. Exploded assembly of the Single Element TES Device.

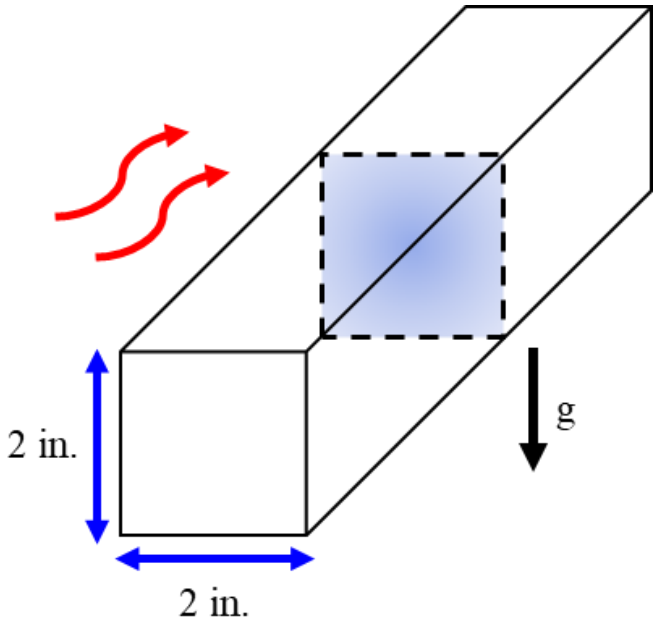

Figure 2-2. Cross section of the square tube TES element.

2.2 ROC Composition

The ROC is composed of the solid remains from a desalination process, therefore it contains the dissolved salts from the water source. Typically, the water source comes from salty and brackish water systems that contain salts grouped into chlorides, carbonates, sulfates and hydroxides. NaCl, or commonly table salt, make up the majority of chloride salts. CaCO3, commonly found as calcite, is one such common carbonate and contributes to the calcium buildup in most homes. MgOH is one such hydroxide component that has also been identified through thermodynamic simulation. The dominating salt species are of particular interest as their bulk properties give information about predicting the thermophysical properties.

Determining these properties requires chemistry analytical data and a thermodynamic software that can predict the precipitation of salt species out of a simulated aqueous solution. The salt sample sourced by the Eastern Municipal Water District, inventoried as ROC10001, was analyzed by Expert Chemical Analysis, Inc (ECA Inc.) for ionic composition. The dominant anions were chlorides, bicarbonates, and sulfates. The dominant cations were sodium, calcium, magnesium, and potassium. This data was then analyzed using water chemistry techniques outlined in [13] to estimate the composition of the different molecules that make up the ROC. The outcome of these formulas was a mass ratio of the dominant solid phase species summarized in Table 2-1. This composition was then used to determine the thermophysical properties, thus being one step closer to characterizing its heat transfer behavior.

Table 2-1. Approximate chemical composition of ROC10001.

Component	Chemical Formula	Weight Ratio
Sodium chloride	NaCl	0.45
Calcium carbonate (Calcite)	CaCO3	0.23
Calcium sulfate	CaSO4	0.21
Magnesium hydroxide (Brucite)	Mg(OH)2	0.10

2.3 Thermophysical Properties

Heat transfer analysis of fluids requires thermophysical properties such as density, specific heat capacity, thermal conductivity, and viscosity. For melting simulations additional properties are needed such as the latent heat of fusion and the solidus and liquidus temperature for the range of melting temperature. Determining thermophysical

properties of the EMWD ROC is challenging without the appropriate instruments, and it is expensive to outsource calorimetry, rheology, and thermal conductivity measurements. Quotes from third party measurement vendors were in the several thousands of dollars citing setup costs as the most significant factor. The setup for calorimetry, via differential scanning calorimetry (DSC), would not be safe on samples with possible volatile organic compounds (VOCs). VOCs are predicted in ROC given the natural source of water. The setup for viscosity, via a rheometer with furnace, is also cost prohibitive because of corrosion concerns; requiring a new cup and bob for each sample. Thermal conductivity was also costly for setup with suspending the substance in an epoxy resin and also citing VOCs as safety concern. Melting point and density remain as the only two economically determinable properties. The rest are determined by weighted averaging of the pure components.

Melting experiments have been performed using two methods. First with propane torches heating a crucible in a container molded using refractory cement such as the setup in Figure 2-3. This is a fast and affordable method of observing when melting occurs, however it is not suitable for finely controlled heating temperature nor is it permitted for indoor experiments. The second method for heating a sample is to repurpose an electric furnace meant for melting jewelry metals to melt ROC. The setup in Figure 2-5 shows the electric furnace and thermal probes that measure the temperature of the ROC and outside of the crucible.

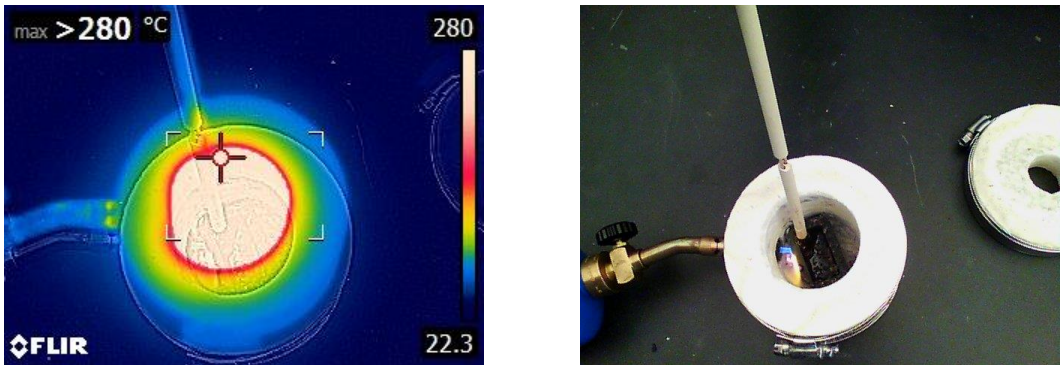

(a) (b)

Figure 2-3. Thermal camera image (a) of melting with propane torch setup (b).

Many pure substances have well documented thermophysical properties that are available in many databases accessible through the internet or textbooks, however the estimating of properties for mixtures presents a great challenge. Some salt mixtures exist as binary and sometimes tertiary mixtures of commonly desired TES salt mixtures. Solar salt is an example of a commercially available salt mixture which is composed of NaNO3 and KNO3 in a 60/40 wt% ratio, respectively, and is primarily used in solar thermal plants such as the Crescent Dunes Solar Power Tower Plant in Nevada. The molten salt reactor project at the Oak Ridge National Laboratory conducted experiments using a tertiary salt mixture, FLiNaK, as a heat transfer fluid for nuclear molten salt reactors. The salt mixture extracted from ROC is more complicated than a binary or tertiary mixture because there are dozens of more components present and many more theoretically predicted. The ROC also is not derived from pure substances in controlled weight ratios, so the complication of identifying species and quantifying their amounts becomes unknown variables that are not easy to determine. Nonetheless there must be a way to predict thermophysical properties of ROC to proceed with product design.

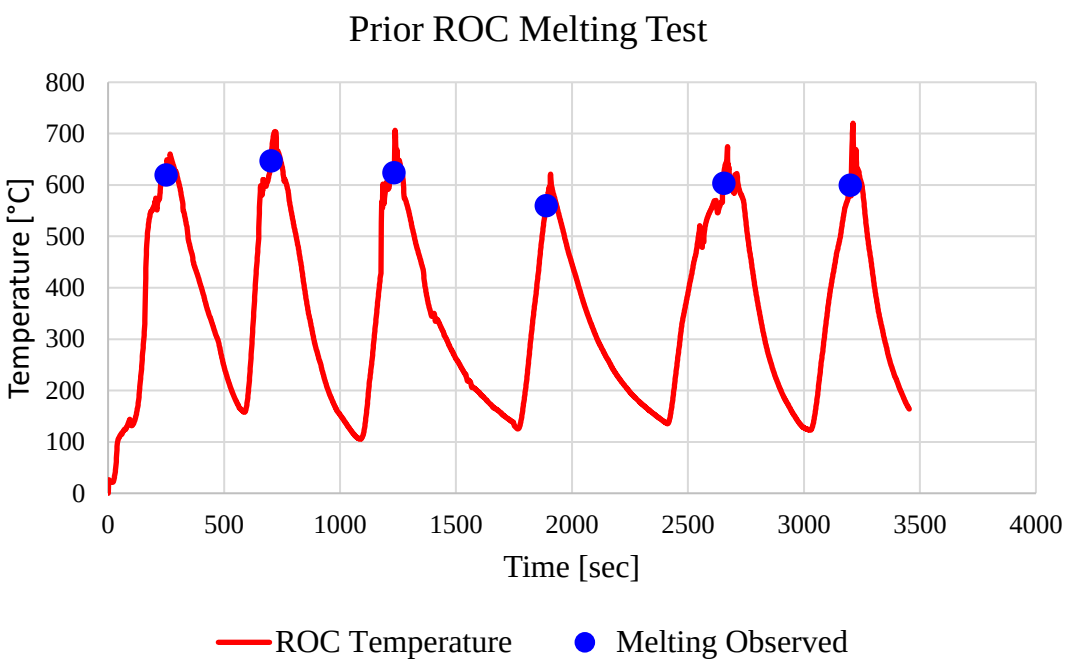

Figure 2-4. Melting test of ROC10001 from torch melting experiment.

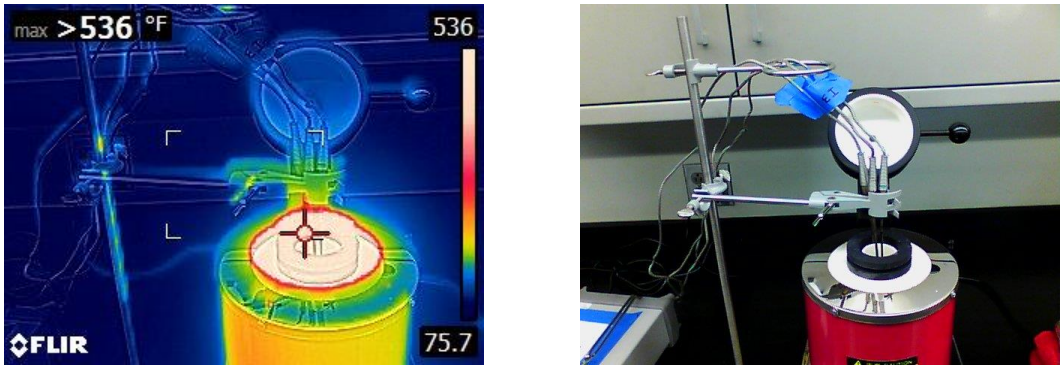

(a) (b)

Figure 2-5. Thermal camera image (a) of melting with electric furnace setup (b).

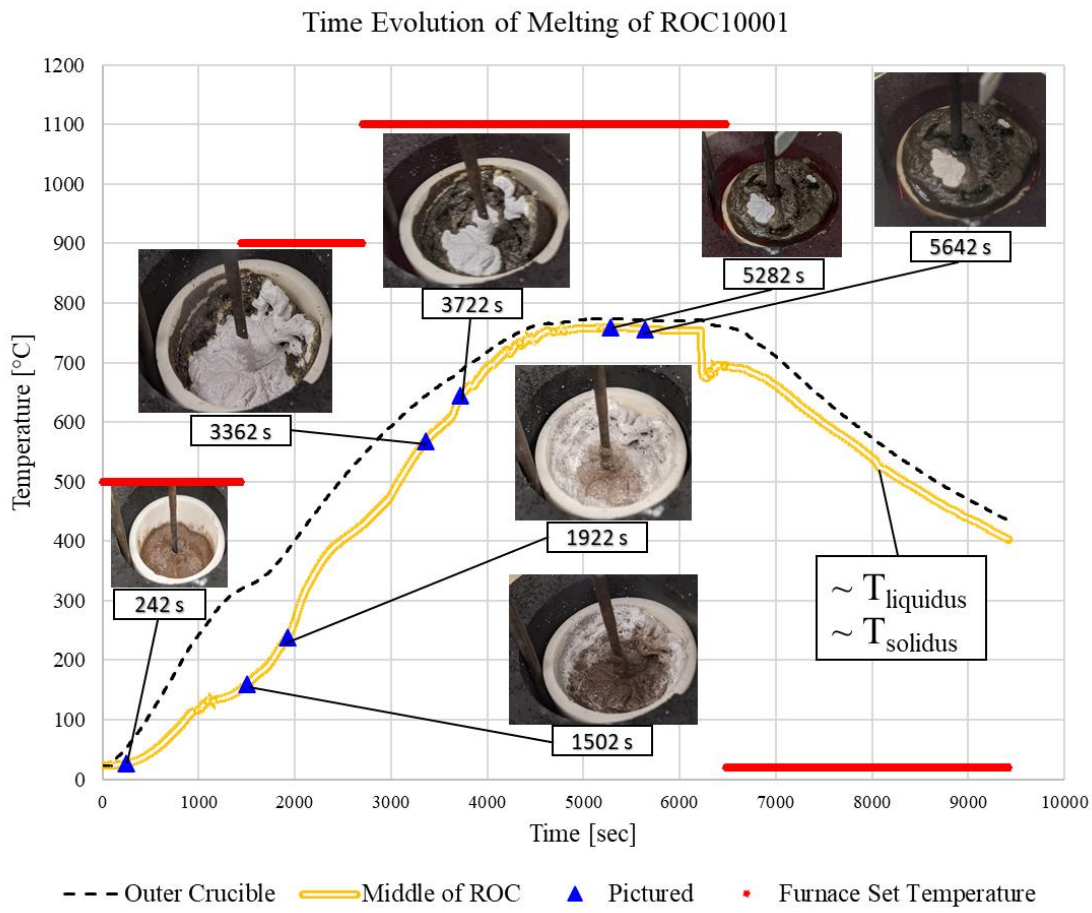

Figure 2-6. Time evolution of melting of ROC10001 in electric furnace.

Weighted averaging of each salt species and estimating their weighted average thermophysical properties allows for their properties to be entered into an ANSYS Fluent material database and simulate heat transfer behavior. Eq.1. shows how the weighted average is the sum of all *n* components the product of mass fraction y_i, multiplied by the ith property $W_i(T)$, where W is for either density, heat capacity, thermal conductivity, and viscosity. Comparing the thermophysical property of each substance independently, such as specific heat capacity, the outcome is that there is a range for that property to fall in between the minimum and maximum value.

$$W(T) = \sum_{i}^{n} y_i W_i(T) \quad (1)$$

Table 2-2. Temperature-independent, weighted average properties of ROC10001.

Property	Value	Units
$T_{solidus}$	873.374	[K]
$T_{liquidus}$	896.925	[K]
Latent Heat of Fusion	314116	[J/kg]

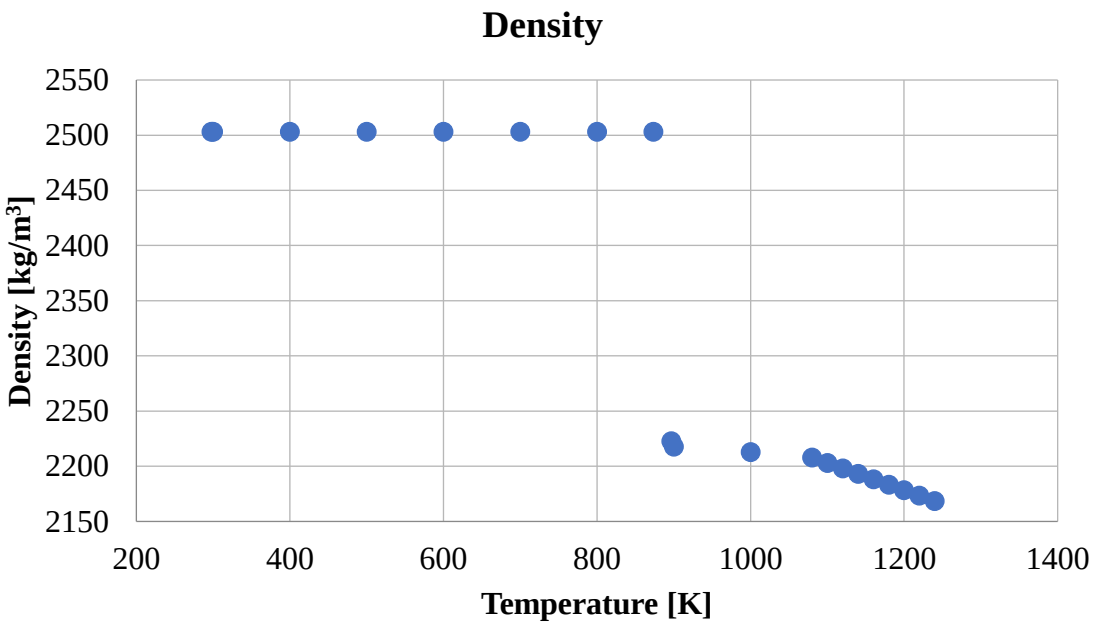

Figure 2-7. Temperature dependent density of ROC10001.

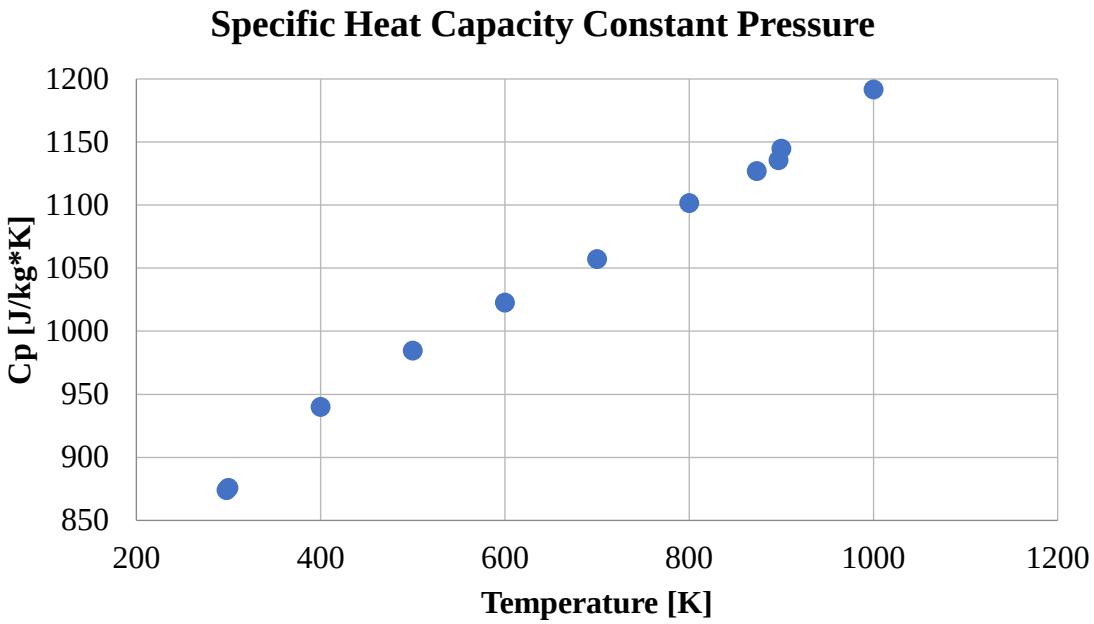

Figure 2-8. Temperature dependent specific heat capacity of ROC10001.

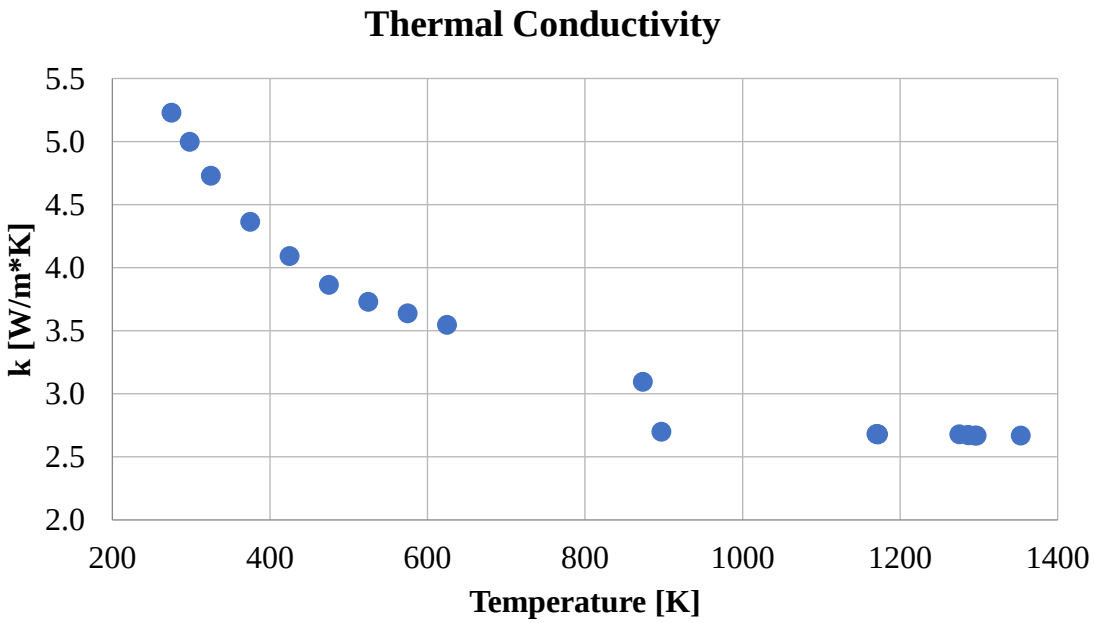

Figure 2-9. Temperature dependent thermal conductivity of ROC10001.

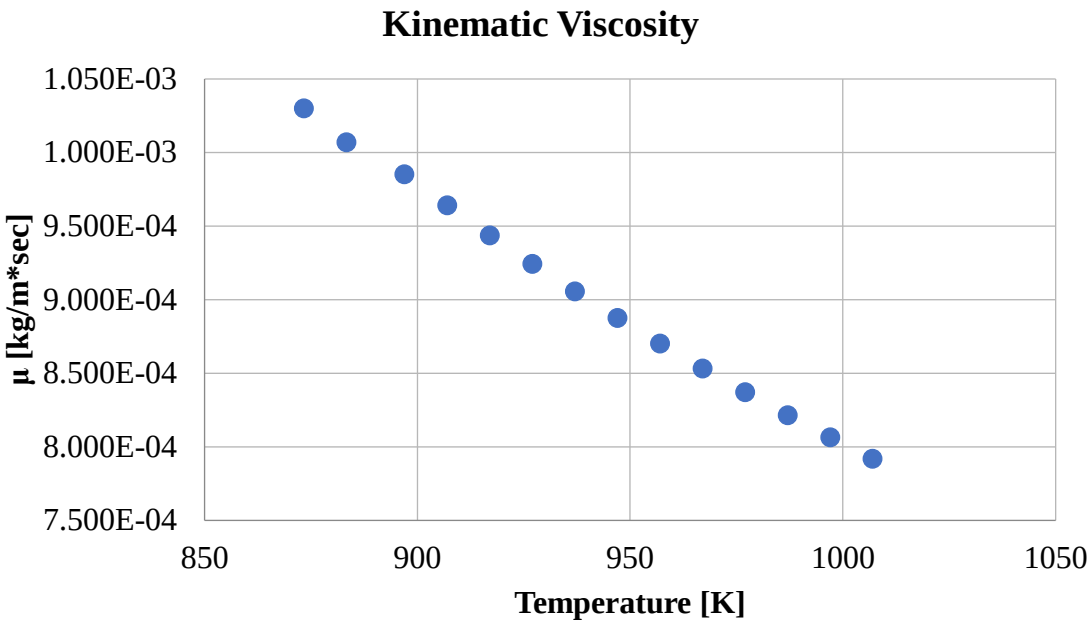

Figure 2-10. Temperature dependent kinematic viscosity of ROC10001.

The thermophysical properties listed in Table 2-2 and plotted on Figure 2-7, Figure 2-8, Figure 2-9, and Figure 2-10 were entered into Fluent as singular values and also piecewise linear data with temperature dependency. These sets of property data allow for Fluent to interpolate in between values to make simulations that approximate the real world heat transfer effects.

2.4 Governing Equations

The governing equations are a set of differential equations shown in Eqs 2,3, and 4 which represent the general vector form of the continuity, momentum, and energy equations respectively as listed in the ANSYS Fluent Theory Guide [14]. The conservation of mass is solved by the continuity equation shown in Eq 2. The

conservation of momentum is solved by Eq 3, which has also been referred to as the Navier Stokes Equation, and this equation determines the velocity profile. The conservation of energy is solved by the energy equation in Eq 4 , which determines the temperature profile. Together these three solve the velocity and temperature at each mesh cell volume, and ANSYS Fluent solves these equations numerically and iteratively. The equations are calculated in an iterative fashion until all user-defined error criteria, or residuals, are met. The equations listed after these governing equations are enhancements to the three main governing equations where each equation modifies terms in the momentum and energy equations. The main focus of this study is to learn how temperature and velocity are coupled as a result of buoyancy driven flow and the equations that couple the momentum and energy equations will be discussed.

$$\frac{\partial}{\partial t}(\rho) + \nabla \cdot (\rho \vec{v}) = 0 \tag{2}$$

$$\frac{\partial}{\partial t}(\rho \vec{v}) + \nabla \cdot (\rho \vec{v}\vec{v}) = -\nabla p + \nabla \cdot (\bar{\bar{\tau}}) + p\vec{g} + \vec{F} \tag{3}$$

$$\frac{\partial}{\partial t}(\rho E) + \nabla \cdot [\vec{v}(\rho E + p)] = \nabla \cdot \left[k\nabla T - \sum_j h_j \overrightarrow{J_j} + (\bar{\bar{\tau}} \cdot \vec{v}) \right] \tag{4}$$

The driving force of natural convection is the magnitude of the buoyancy force term, $p\vec{g}$, where the density of the ROC changes according to a piecewise linear data set. The presence of gravity in a fluid domain with a density gradient causes the hotter, lesser dense fluid to rise against the direction of the gravitational acceleration and consequently pushes at the cooler, denser fluid. This forms a coupled relationship between the energy and momentum equations since the temperature of the fluid solved by the energy equation determines the buoyancy term in the momentum equation.

Before the ROC, or any other PCM, experiences fluid motion, it must first overcome the energy required to undergo a phase change from solid phase to liquid phase. Many pure substances have narrow melting temperature ranges, but the salt hydrates have a larger phase change temperature range rather than a single temperature [15]. Likewise, PCMs are shown to reach complete melting over a temperature range as opposed to a single temperature [16]. Fluent uses the enthalpy-porosity technique to simulate melting, where the melting interface is tracked implicitly using the liquid fraction of each cell [17] [18] [19]. The use of the enthalpy-porosity technique has also been explored for buoyancy driven melting [20]. The enthalpy, in Eq.5., takes into account the sensible enthalpy and latent heat. Determining when phase change has occurred relies on the calculation of the liquid fraction at a particular cell volume. The liquid fraction is the normalized proportion of liquid phase in each cell volume computed at each iteration based on the enthalpy balance. The liquid fraction is calculated by Eq.7. where liquid fraction of 0 indicates solid phase, a 1 indicates liquid phase, and any value in between is defined as the mushy zone. The mushy zone is modeled as a porous medium [9], which allows velocity to be greater than zero in the mushy zone. Once the liquid fraction is solved by Eq 7, the latent heat in Eq 5 is updated.

$$\mathrm{H} = \mathrm{h} + \Delta\mathrm{H} \tag{5}$$

$$h = h_{ref} + \int_{T_{ref}}^{T} c_p dT \tag{6}$$

$$\beta = \begin{cases} 0 & if \quad T_S > T \\ \dfrac{T - T_S}{T_L - T_S} & if \quad T_S < T < T_L \\ 1 & if \quad T > T_L \end{cases} \tag{7}$$

$$\Delta H = \beta L \tag{8}$$

Modeling of solidification and melting changes the energy equation from Eq.4. to Eq.9. which introduces the momentum sink, S, as a source term from Eq.10, which accounts for the loss in momentum as the porosity is reduced. The Voller and Swaminathan method [19] is used to solve iteratively between Eq 7 and Eq 9 to improve convergence.

$$\frac{\partial}{\partial t}(\rho H) + \nabla \cdot [\vec{v}(\rho H)] = \nabla \cdot [k \nabla T] + S \tag{9}$$

$$S = \frac{(1-\beta)^2}{(\beta^2 + \varepsilon)} A_{mush}\left(\vec{v} - \vec{v}_p\right) \tag{10}$$

Comparing the charge and discharge cycles according to temperature values is not enough to get a relative sense of progress. The normalized or nondimensionalized form of temperature is used to relate the progress of the charge or discharge cycles. The variable T*, or sometimes written as θ, expressed in Eq.11. is the ratio of the current average temperature of the fluid minus the initial bulk fluid temperature over the constant surface temperature minus the initial bulk fluid temperature. The difference between the surface temperature and the initial bulk fluid temperature is the greatest difference present in either cycle. The nondimensional form of temperature allows for analysis of performance of the charge and discharge cycles by comparing the duration of when T* is between 0.1 and 0.9.

$$T^* = \frac{T - T_{\infty,i}}{T_W - T_{\infty,i}} \tag{11}$$

TES is inherently a transient heat transfer process that is changing the total temperature of the system over time. A transient heat transfer model can be used to determine the temperature of the system given a specified time and vice versa. The lumped capacitance model, shown in Eq.12., is a simplified transient heat transfer model that can be used to estimate the internal temperature inside a TES device. This model serves as a validation for the temperature change during simulation.

$$\frac{T - T_\infty}{T_i - T_\infty} = exp\left[-\left(\frac{h_c A_s}{\rho V_c}\right)t\right] \tag{12}$$

2.5 Boundary and Initial Conditions

The simple 2D geometry of the PCM element allows for modeling of simple boundary and initial conditions. The four walls of the square tube are assumed to be the same constant temperature as the air stream for a given cross section. The temperature of the boundary during charging is 700 °C based on the maximum output of hot air from the Heat Torch ™ 200 that is installed on the demonstration device. The charge cycle begins with the solid phase ROC at rest and uniformly 290 °C, then is heated by walls held at constant temperature of 700 °C. The charge cycle ends when the ROC has entirely melted and reached the asymptote temperature of 700 °C and the velocity of the fluid also comes nearly at rest. The discharge cycle begins at the end of the charge cycle with the idealized starting condition of uniform 700 °C temperature and at rest in liquid state. The discharging temperature is 290 °C so that the air will heat another heat transfer fluid for organic Rankine cycle power production [21]. The boundary and initial conditions for the

charge cycle is illustrated in Figure 2-11(a) and the discharge cycle is the reverse of that in (b). Both cycles are assumed to begin when the fluid is at rest, hence the zero velocity at the start. In a scaled out version of this salt element, it is expected that there will be a gradient in the overall average temperature of each cross section spanning the length of the salt tube. These computational results provide an early snapshot of the flow behavior at the leading end of the salt element that will inform how natural convection affects the total heat transfer capabilities at the hottest end other TES device.

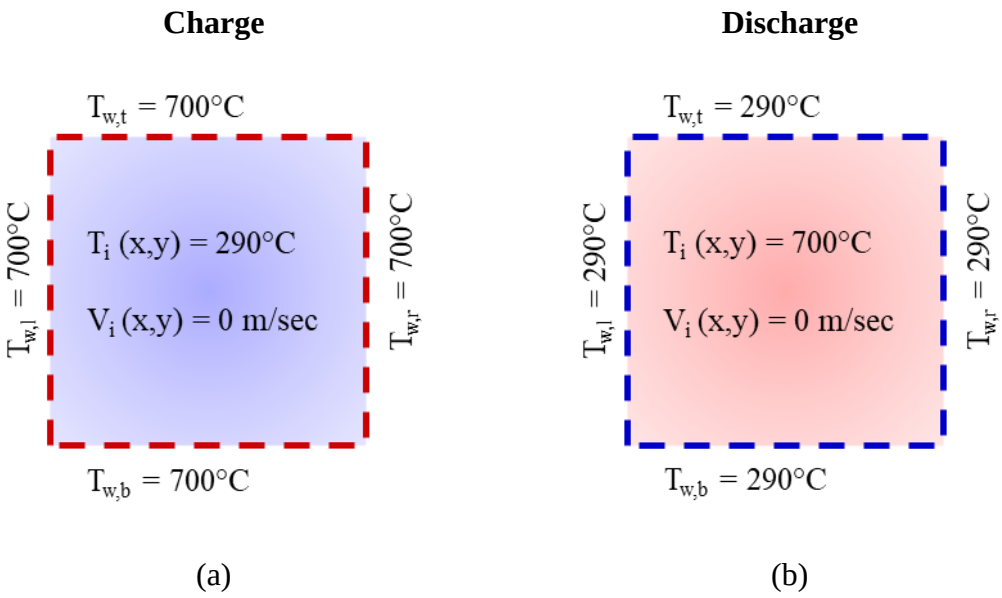

Figure 2-11. Boundary and initial conditions for charge (a) and discharge (b).

2.6 Solver Configuration

Once the mesh was generated and passed to Fluent the boundary and initial conditions could be applied along with the other settings that would enable natural convection through the melting process. The general settings were a transient state solution with gravity enabled at ground level of gravitational acceleration of 9.81 m/sec^2 in the -y direction.

The Rayleigh number was calculated with the assumption of a length scale the full length of the 2 inch enclosure, which came out to be 1.07×10^7. This was considered the maximum Rayleigh number because upon closer analysis of the melting behavior, the highest velocity magnitude occurs in the beginning half of the melting process. It is discussed in further detail in the results and discussion that the effective Rayleigh number would be less than the theoretical value in this TES element filled with liquid phase ROC. With much of the flow obstructed by the remaining solids, the effective Rayleigh number was less, which at a flow time of 100 seconds in the charge cycle the Rayleigh number was calculated at 2.51×10^6 in a certain range that approximates a rectangular enclosure. This also confirms that the laminar flow for viscous model is valid.

The fluid properties were added to Fluent in the form of piecewise linear inputs for each of the temperature dependent properties: density, heat capacity, thermal conductivity, and viscosity. For the repeating of simulations involving this particular set of thermophysical properties of ROC10001, a material database file was exported and used for repeated CFD simulations of this type of analysis and also for another research.

Selection of the solidification and melting model automatically configured the pressure and velocity models to be coupled. It was decided the other solvers were left as second order upwind schemes to come up with more accurate solutions. No other changes were made to the relaxation values. The residuals for transient solutions were kept at 10^{-6} for energy and everything else at 10^{-3}. The time steps needed to be small to converge successfully, so a time step of 0.0025 seconds was applied for each calculation. The important data to export were the calculated volume average values for liquid fraction,

temperature, and heat flux which were available as exportable reports. Specific time step data was also exported to make contour plots of liquid fraction, temperature, and velocity.

2.7 Verification and Validation

To rule out the possibility that the Fluent model was producing bias results due to the mesh structure, a grid refinement test was conducted on meshes that had three times and then nine times the number of meshing elements as the initial 100x100. The mesh for the 3X grid followed a 175x175 square element pattern, and following the same bias factor of 20. The mesh for the 9X followed a 300x300 square element, also having the same bias factor of 20. The 100x100 mesh is shown in Figure 2-12, and likewise the subsequent 3X and 9X meshes look similar with progressively darker lines that cluster the walls. This grid independency test was conducted on a theoretical ROC material under the Boussinesq approximation with constant properties and intended to approximate properties of ROC10001. The methodology and results were published in an ASME2021 paper [22]. Its thermophysical properties are listed in Table 2-3.

Table 2-3. Simplified ROC thermophysical properties for Boussinesq approximation.

ROC Properties, T_{ref} = 814°C	
Solidus Temperature, $T_{solidus}$, [°C]	579.85
Liquidus Temperature, $T_{liquidus}$, [°C]	638.48
Density, ρ, [kg/m^3]	1514
Specific Heat, c_p, [J/kg-K]	1058.35
Viscosity, μ, [kg/m-sec]	0.00103
Thermal Conductivity, k, [W/m-K]	0.497
Thermal Expansion Coefficient, β, [K^{-1}]	0.000345
Pure Solvent Melting Heat, L_m, [J/kg]	520000

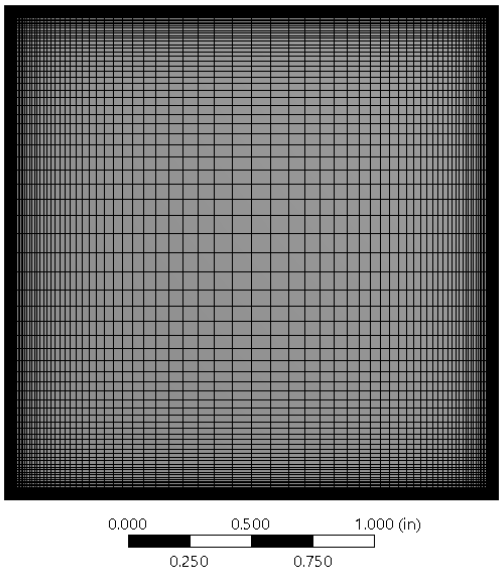

Figure 2-12. Mesh of the 2x2 in. cross section divided into 100x100 edge elements.

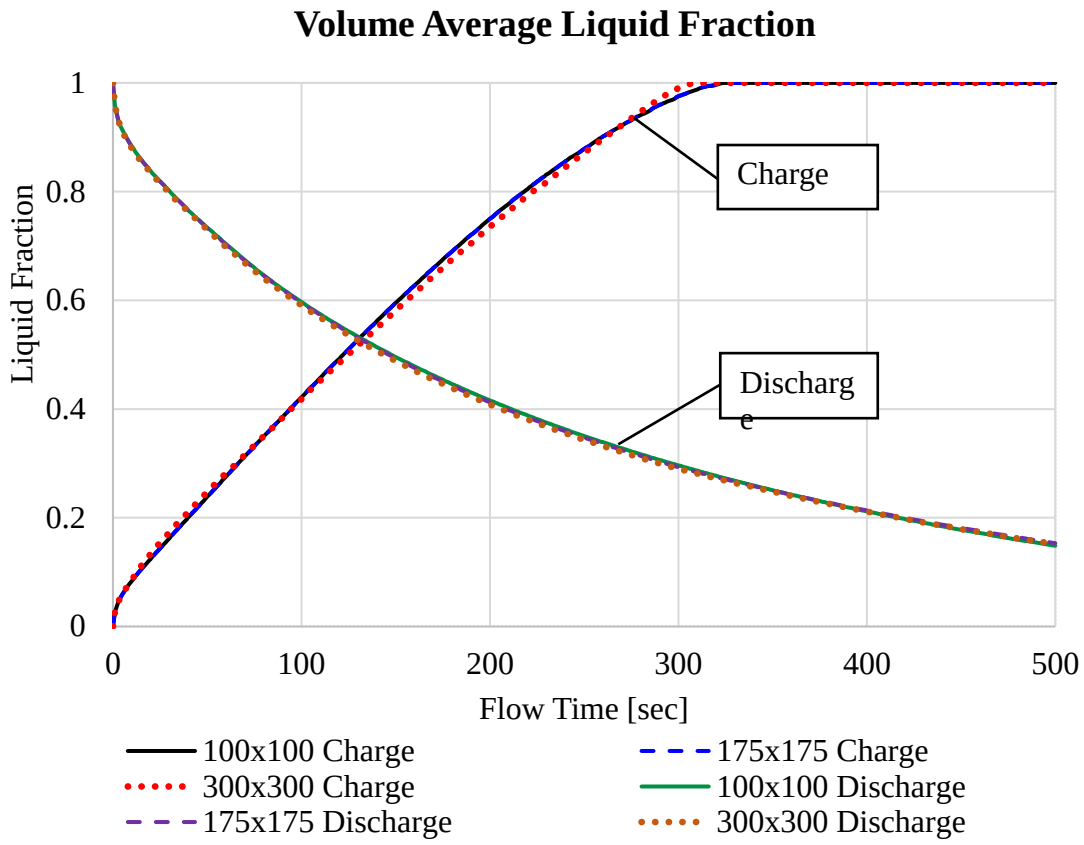

Figure 2-13. Grid independency of liquid fraction for charge and discharge cycles.

The grid refinement results of the ASME paper with the same Fluent setup [22], but with constant fluid properties is shown in Figure 2-13. These quantitative results for liquid fraction of 3X and 9X more than the original showed asymptotic behavior confirming that the results are grid independent. The passing of the grid refinement test shows that the CFD model is verified against bias caused by mesh setup. The verified model was then used on the ROC10001 material that has temperature variable properties. Since the model passed grid independency, the 100x100 grid was used for the remaining contour plots in this thesis.

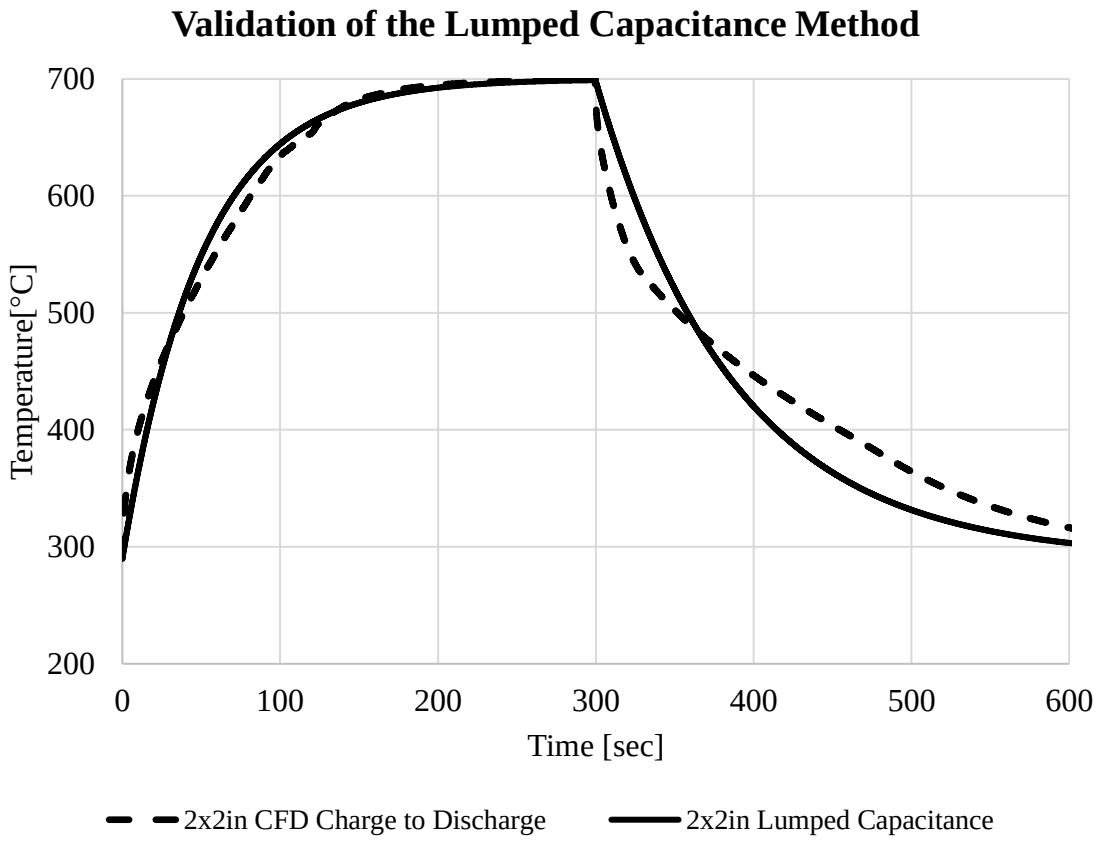

Figure 2-14. Validation with lumped capacitance method. hc = 700, hd = 400 W/m^2-K

A typical heat transfer course introduces the lumped capacitance model as the simplified transient heat transfer scenario. The lumped capacitance assumes that the imbalance of the heat exchange leads to a transient heat transfer problem. During the charge cycle the constant 700°C boundary condition is made possible by convective heat transfer of hot air to the TES element container. The same scenario is true for during the discharge cycle where the constant 200°C boundary condition is due to convection of cool air. Figure 2-14 shows the plot of the average temperature simulated in Fluent versus

the hand calculated temperature following the lumped capacitance method. The model works best if convection heat transfer coefficient of the charge cycle is hc = 700 W/m^2-K, and for discharge hd = 400 W/m^2-K. The maximum relative error of the charge cycle is 10%, and for the discharge cycle is 14%. The lumped capacitance serves as a validation of the duration of melting ROC in an enclosed container. Acceptance of the lumped capacitance method as a validation model is based on this being an early model for heat storage and that the thermophysical properties are yet to be complete.

CHAPTER 3 RESULTS AND DISCUSSION

3.1 Timelapse of Melting and Solidification

A useful visual for understanding the melting and solidification of any substance is the timelapse using a contour plot. The temperature contour plot is an appropriate illustration of the effects of the temperature gradient at the mushy zone and it can also visualize some flow activity. Starting at 20 seconds into the charge cycle, in Figure 3-3, shows formation of vortices at the bottom corners where the corners melted sooner. Once enough ROC has melted there are some unsteady vortex formations happening at the bottom surface in Figure 3-5 at 100 seconds.

The discharge cycle timelapse shows the solidification of ROC forming on the side walls which encapsulates the remaining liquid. Solidification formation of an insulating layer has advantages in other power generation cycles such as the plugging of nuclear molten salt reactors [23], however this may pose as a disadvantage for TES devices for faster discharge duration. There is some fluid flow activity which can be seen by some vortices in the corners in Figure 3-10 for 10 seconds and Figure 3-11 for 20 seconds into the flow time. This is a short duration of any flow activity as the remaining time in the solidification process does not reveal indication of flow activity. This suggests that the insulating effects also slow down buoyancy driven flow and the heat transfers through the liquid conductively rather than convectively.

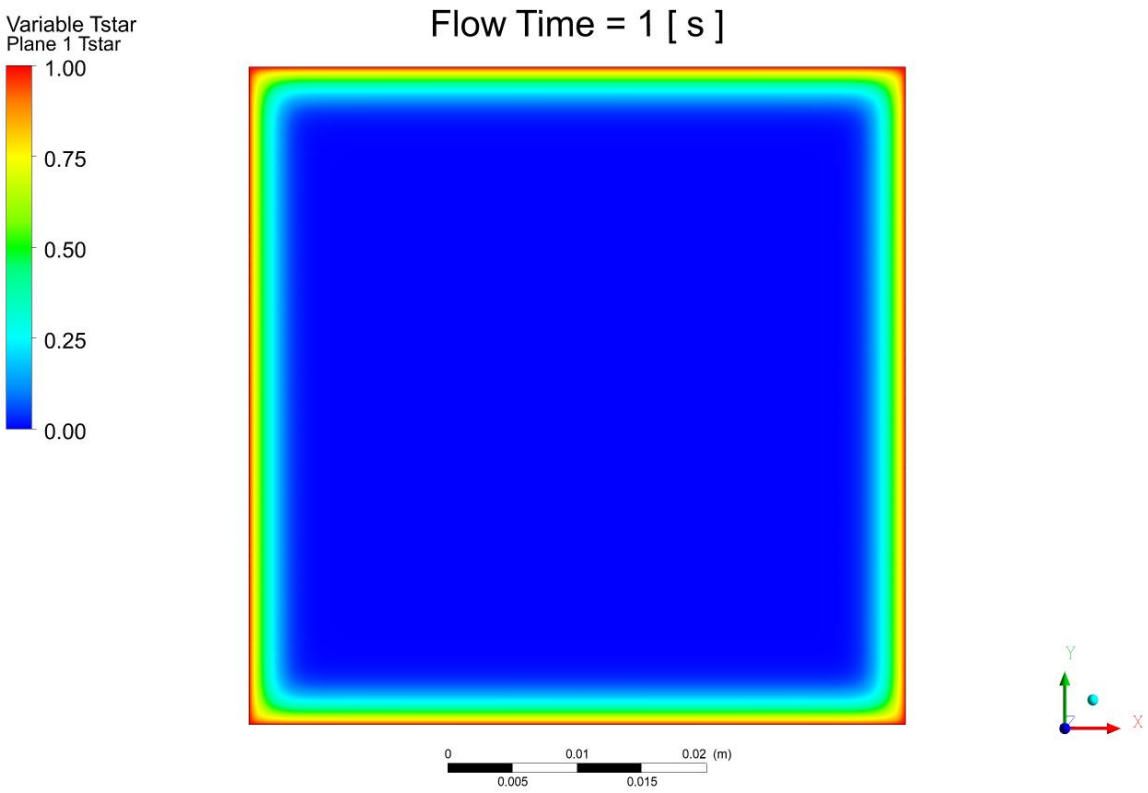

Figure 3-1. Charge cycle dimensionless temperature at 1 second.

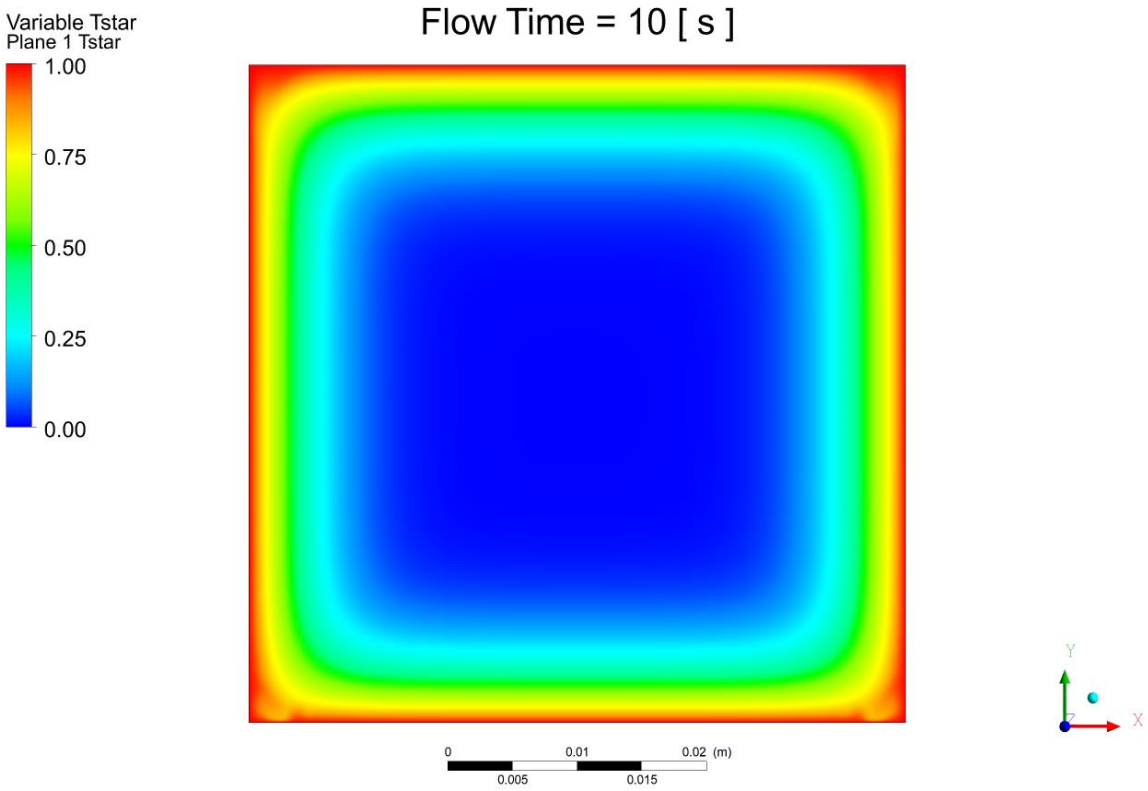

Figure 3-2. Charge cycle dimensionless temperature at 10 seconds.

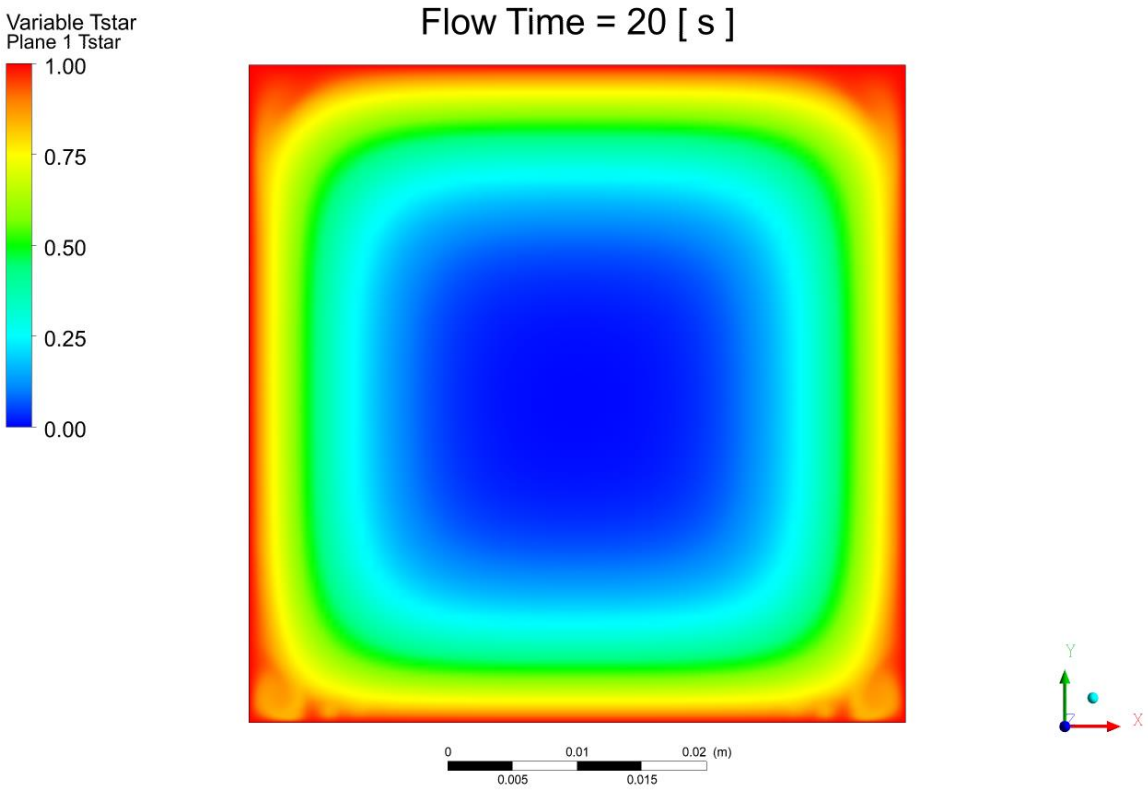

Figure 3-3. Charge cycle dimensionless temperature at 20 seconds.

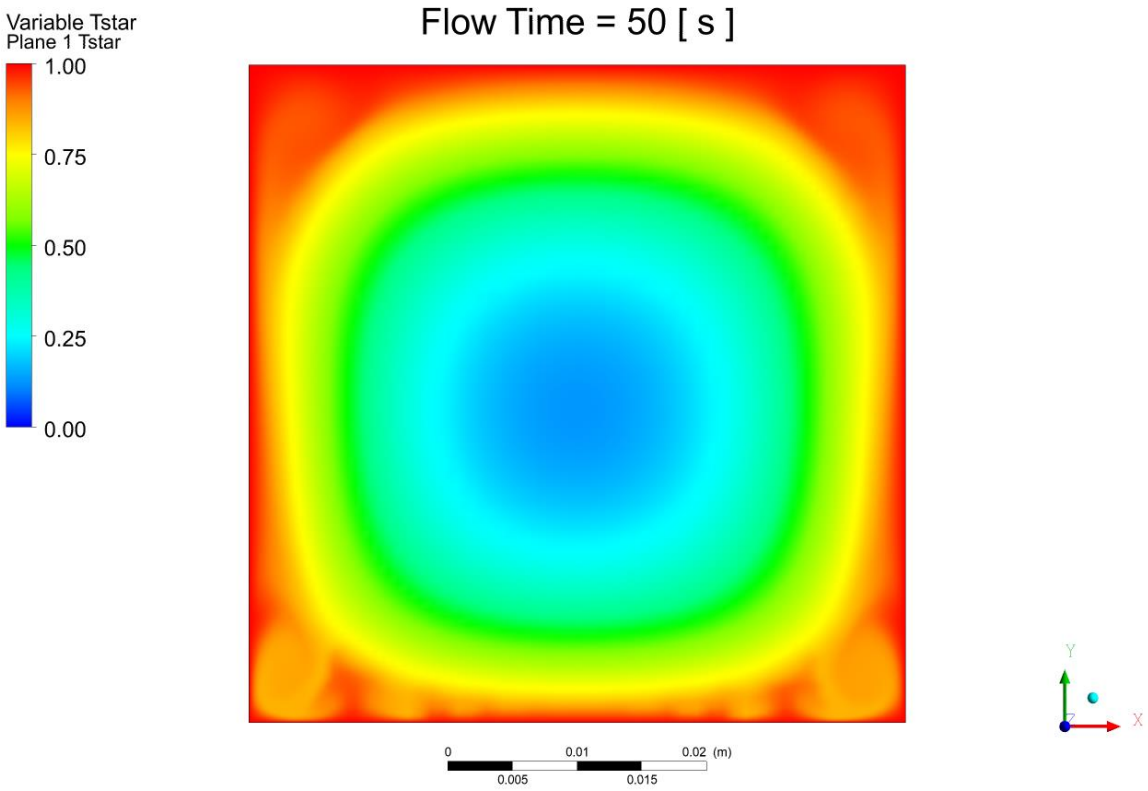

Figure 3-4. Charge cycle dimensionless temperature at 50 seconds.

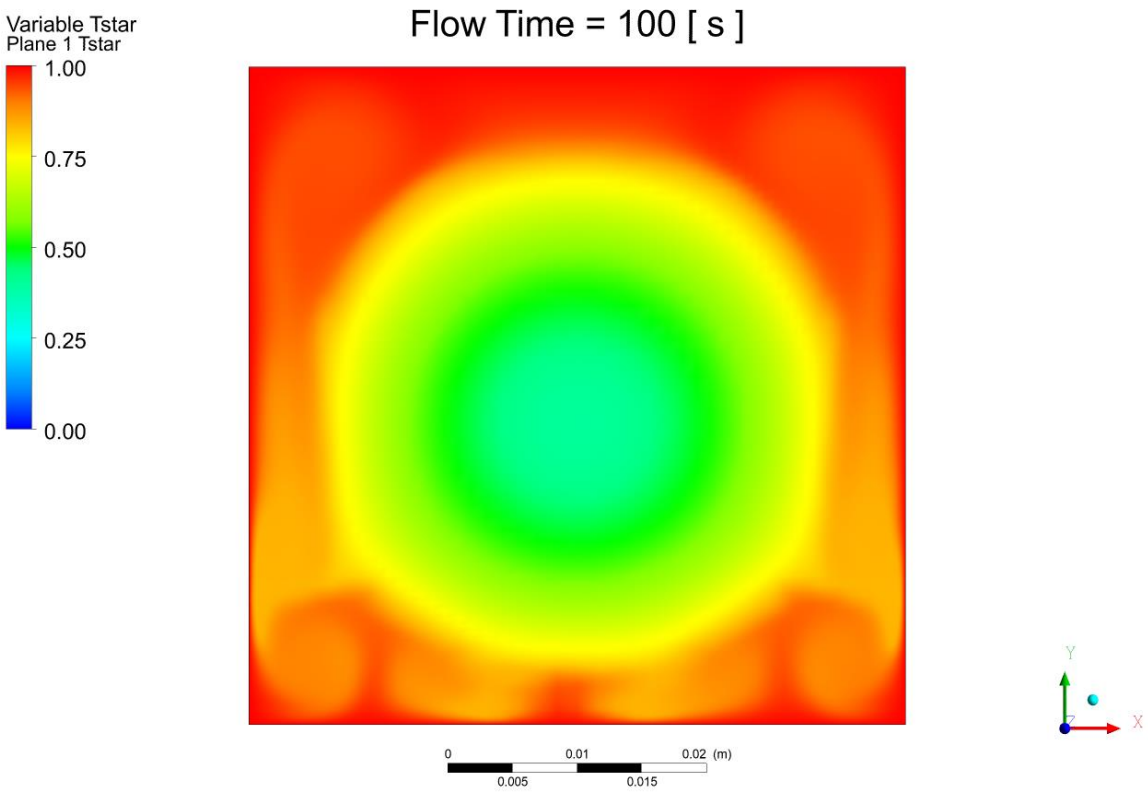

Figure 3-5. Charge cycle dimensionless temperature at 100 seconds.

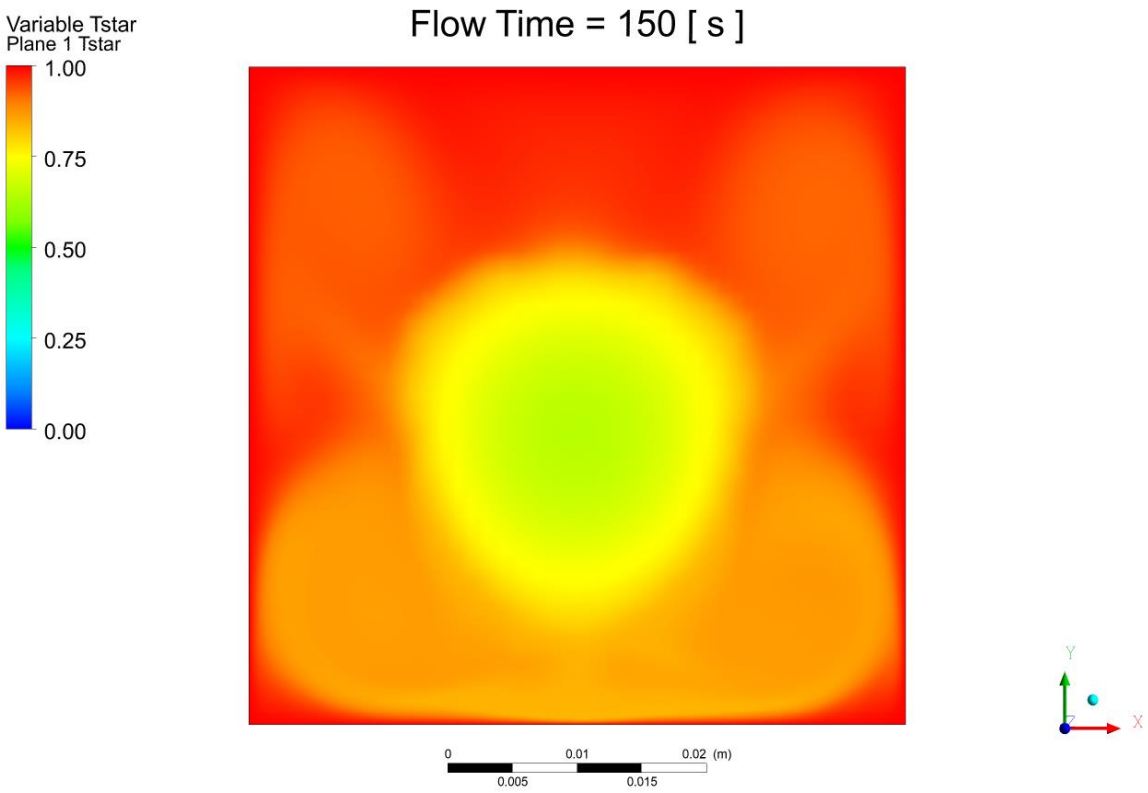

Figure 3-6. Charge cycle dimensionless temperature at 150 seconds.

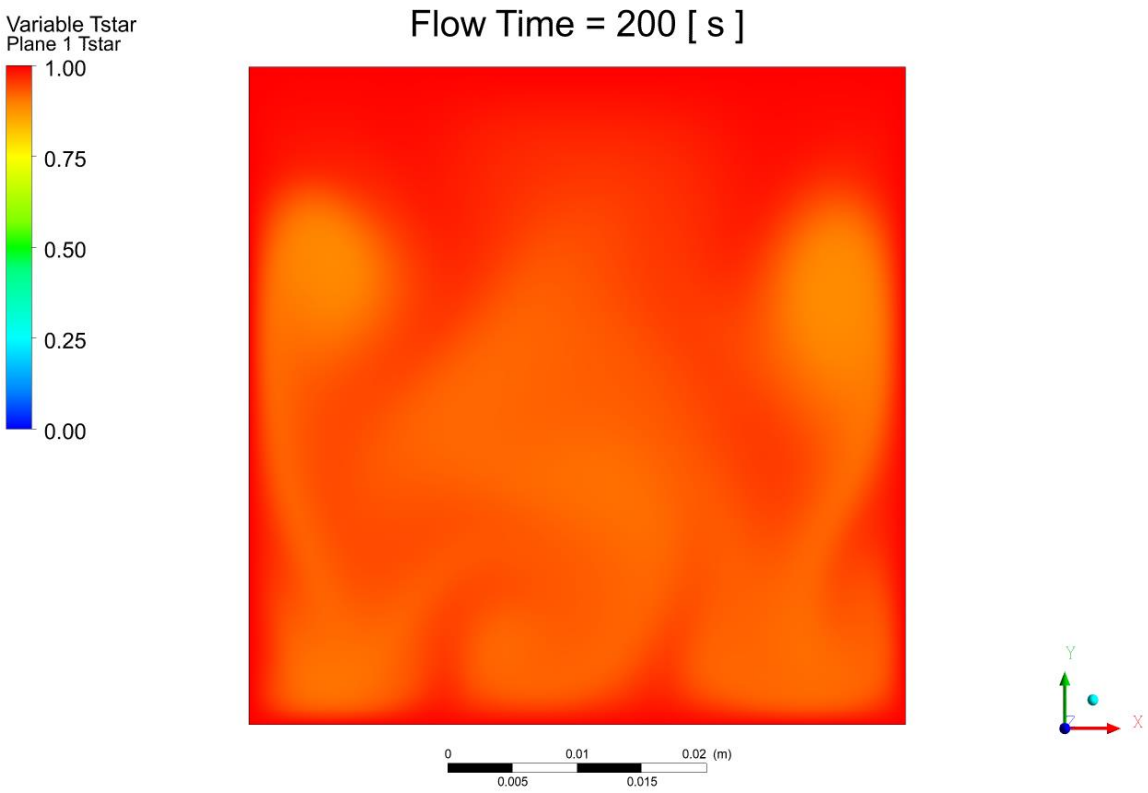

Figure 3-7. Charge cycle dimensionless temperature at 200 seconds.

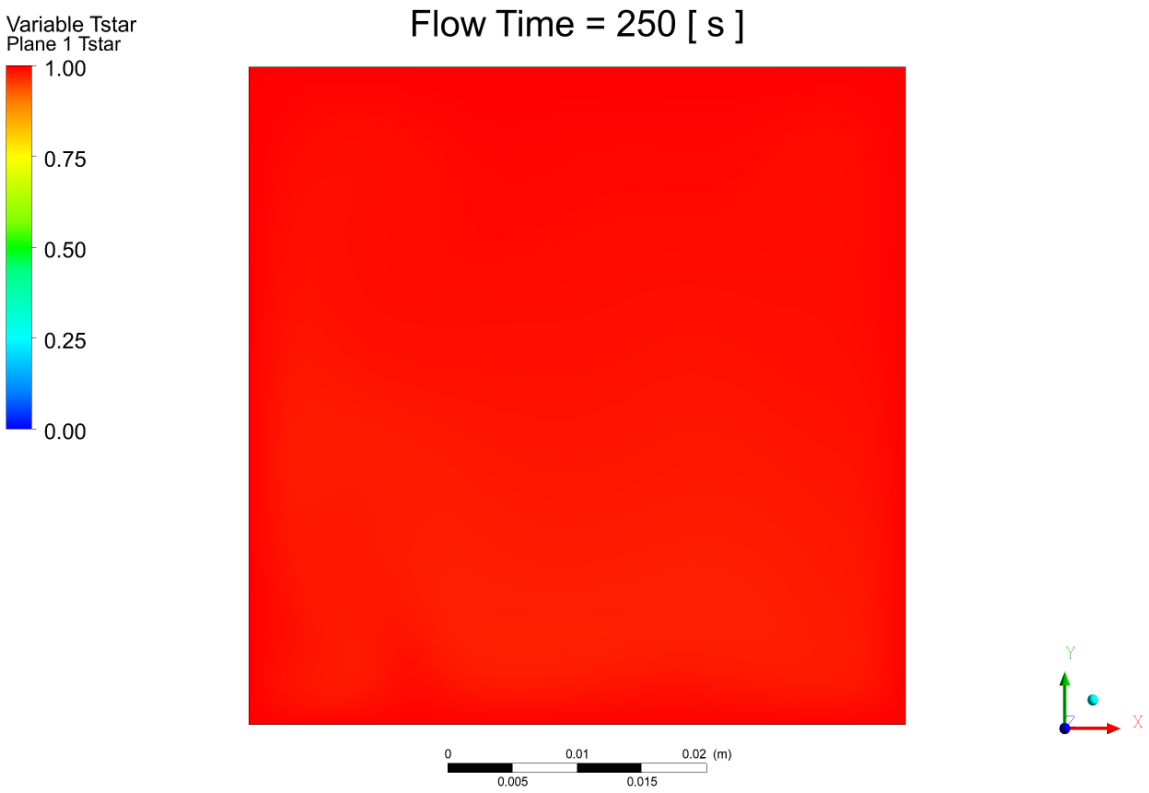

Figure 3-8. Charge cycle dimensionless temperature at 250 seconds.

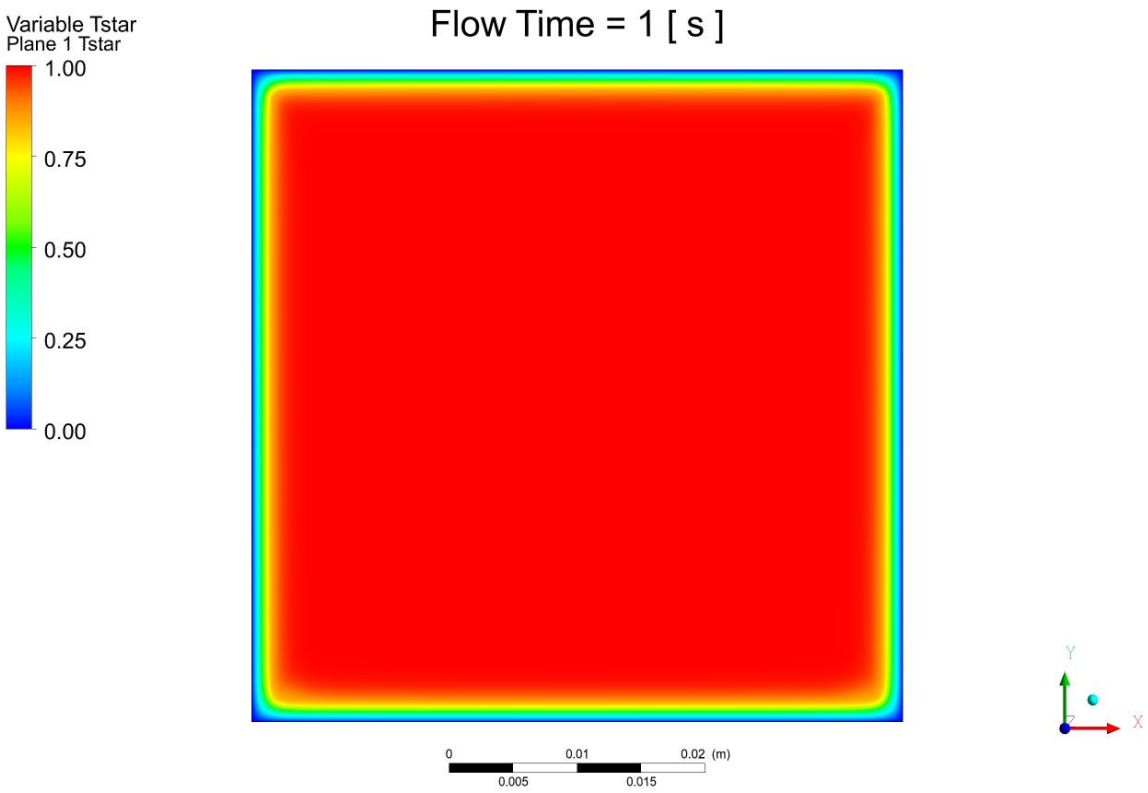

Figure 3-9. Discharge cycle dimensionless temperature at 1 second.

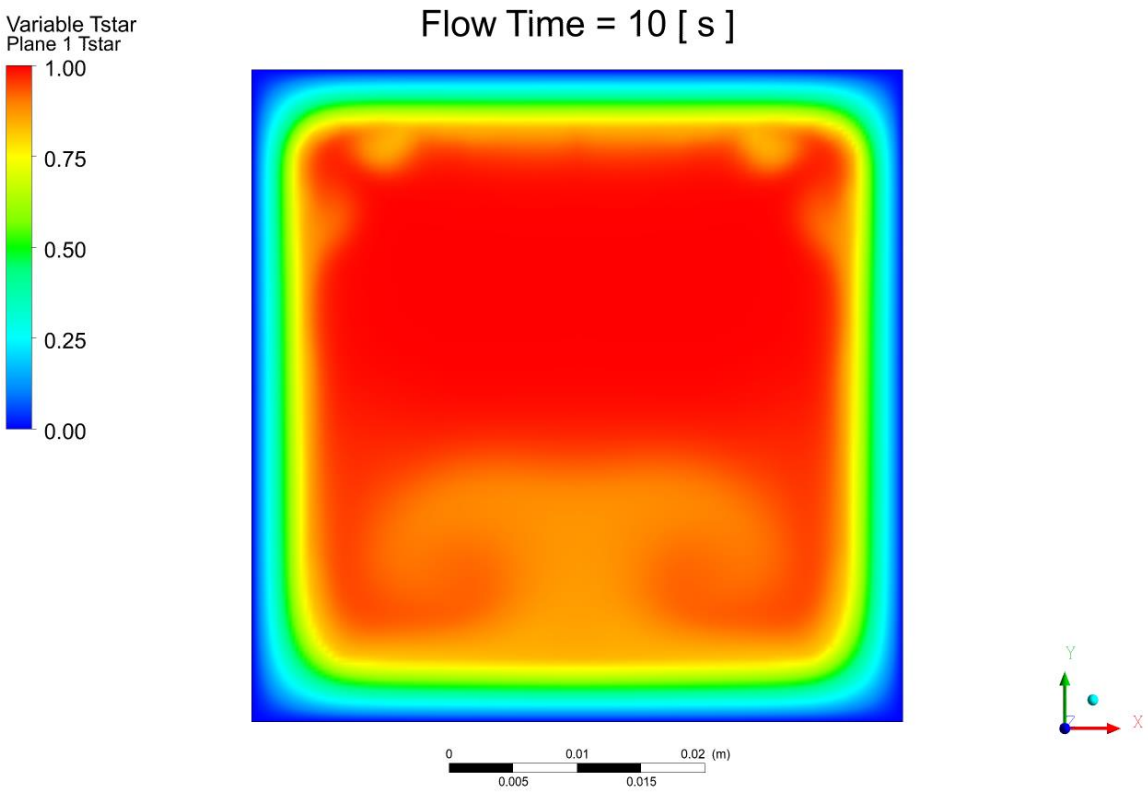

Figure 3-10. Discharge cycle dimensionless temperature at 10 seconds.

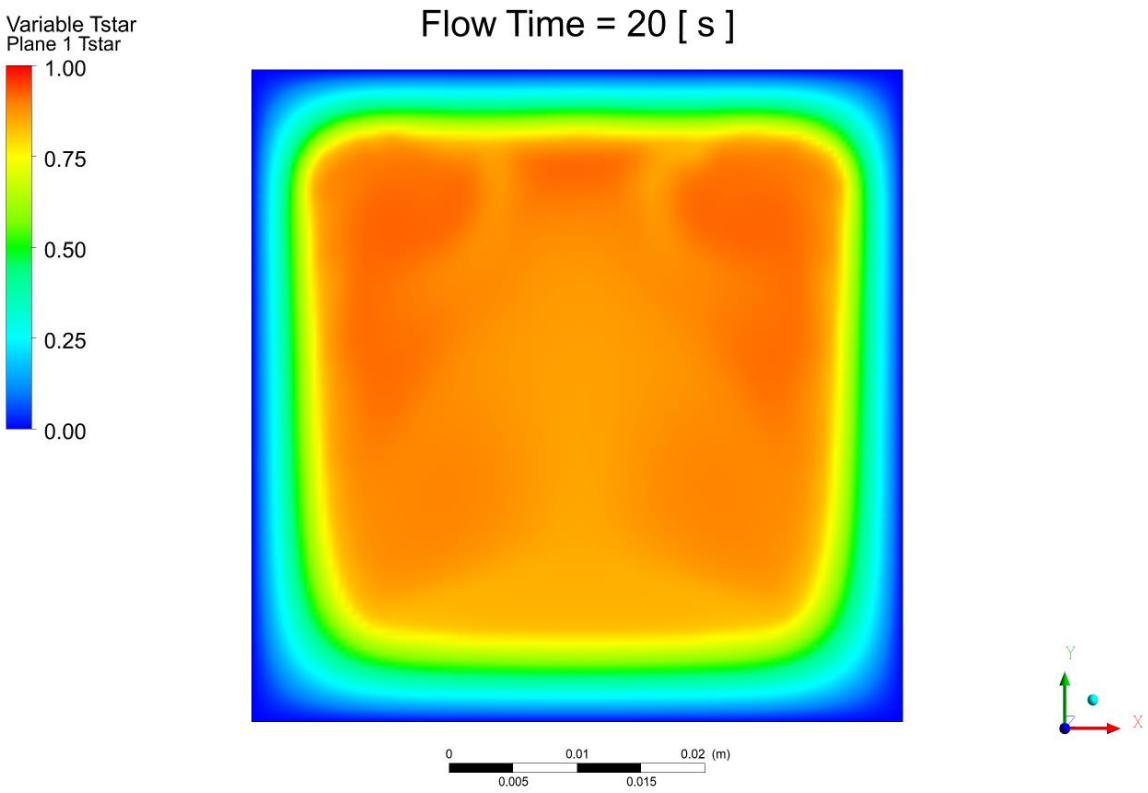

Figure 3-11. Discharge cycle dimensionless temperature at 20 seconds.

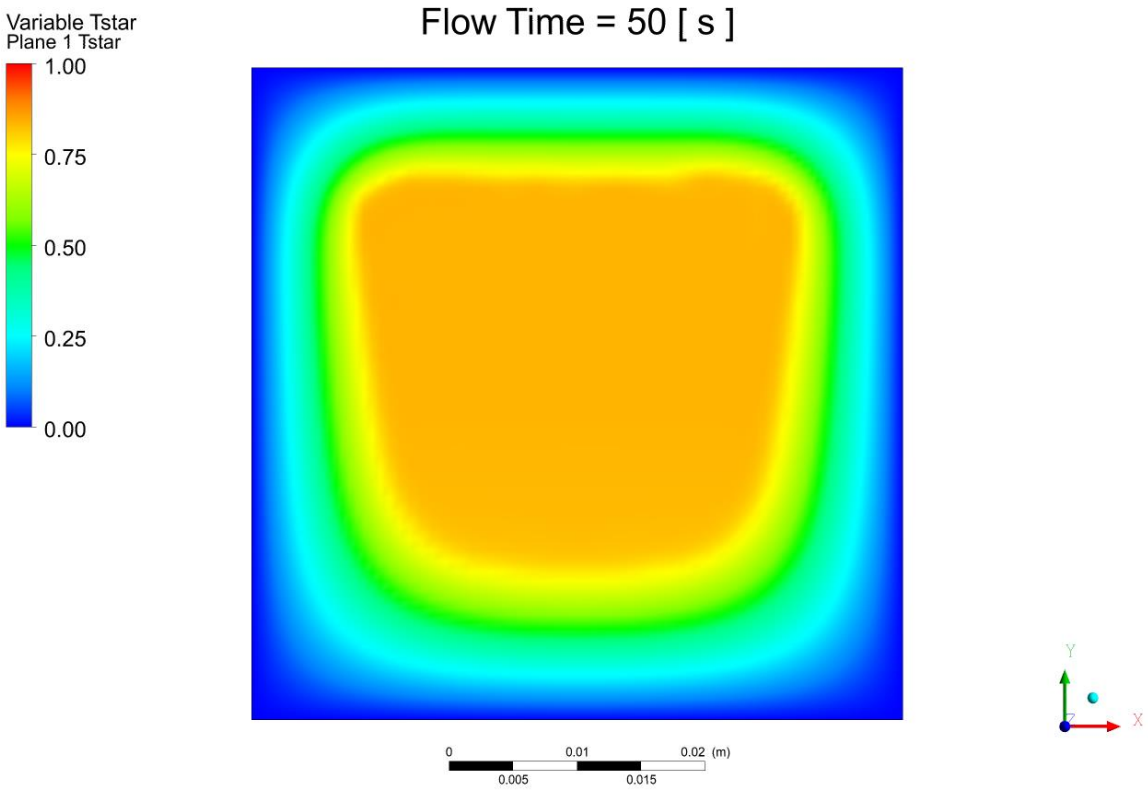

Figure 3-12. Discharge cycle dimensionless temperature at 50 seconds.

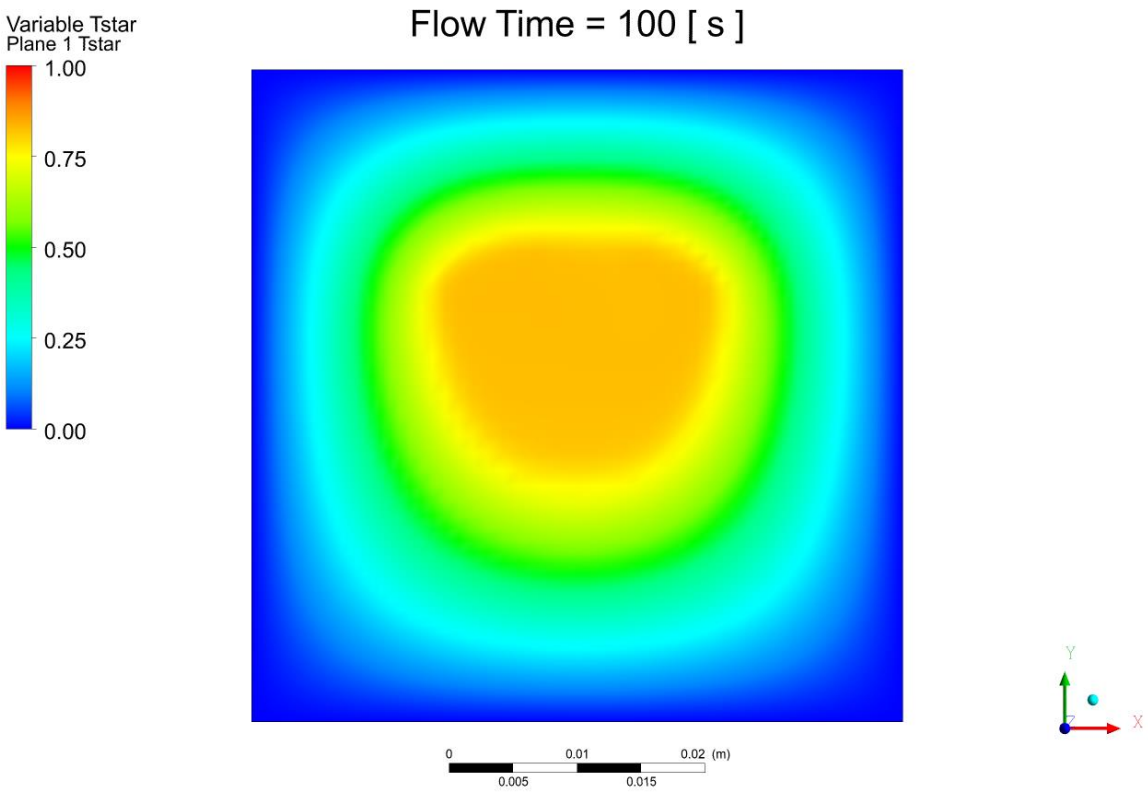

Figure 3-13. Discharge cycle dimensionless temperature at 100 seconds.

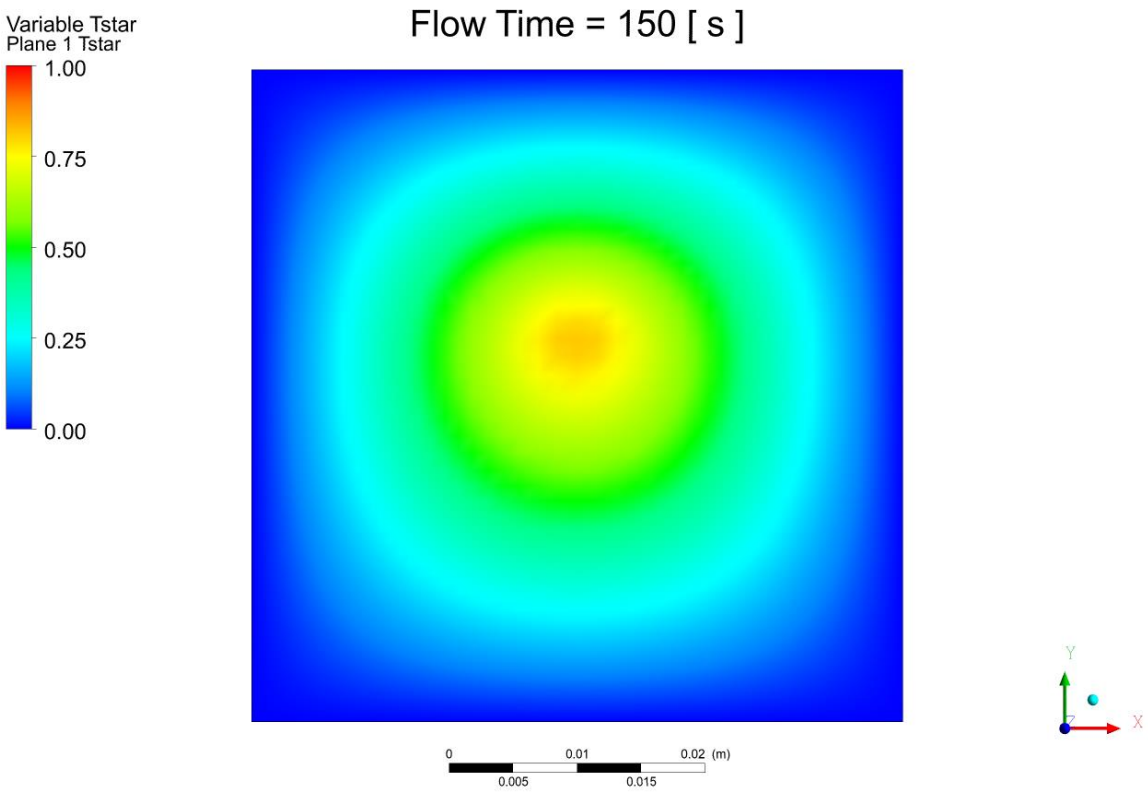

Figure 3-14. Discharge cycle dimensionless temperature at 150 seconds.

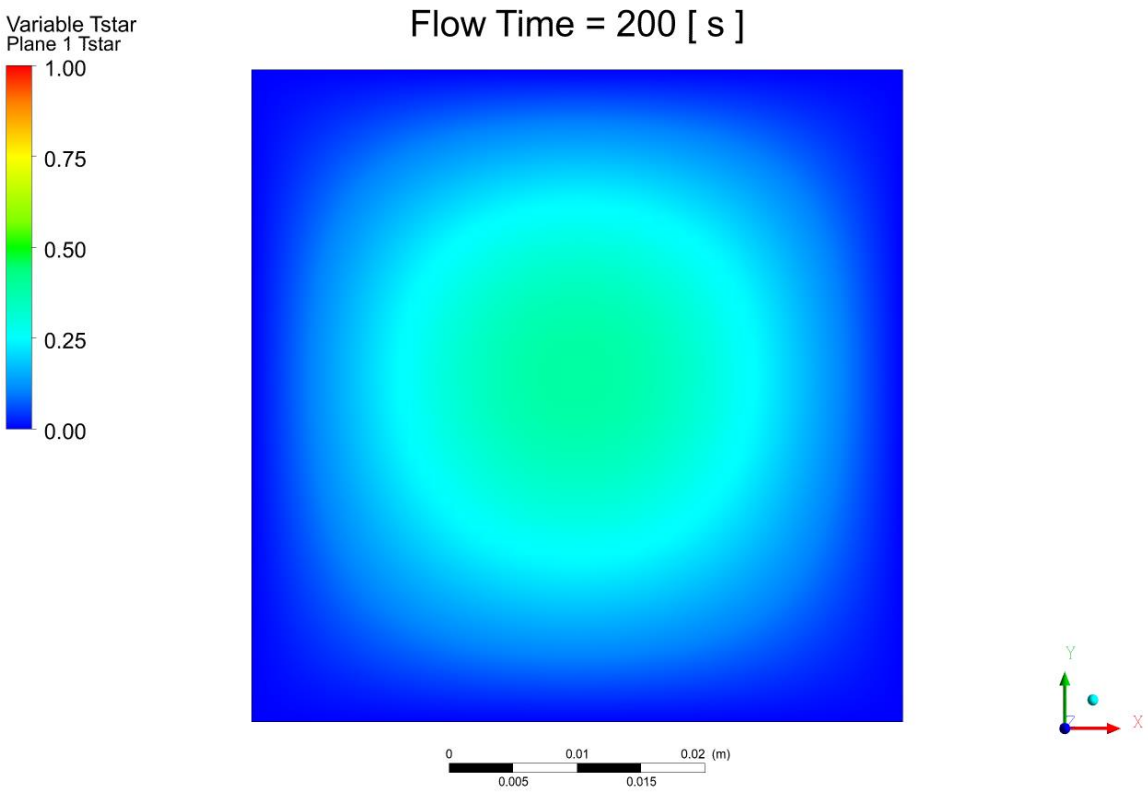

Figure 3-15. Discharge cycle dimensionless temperature at 200 seconds.

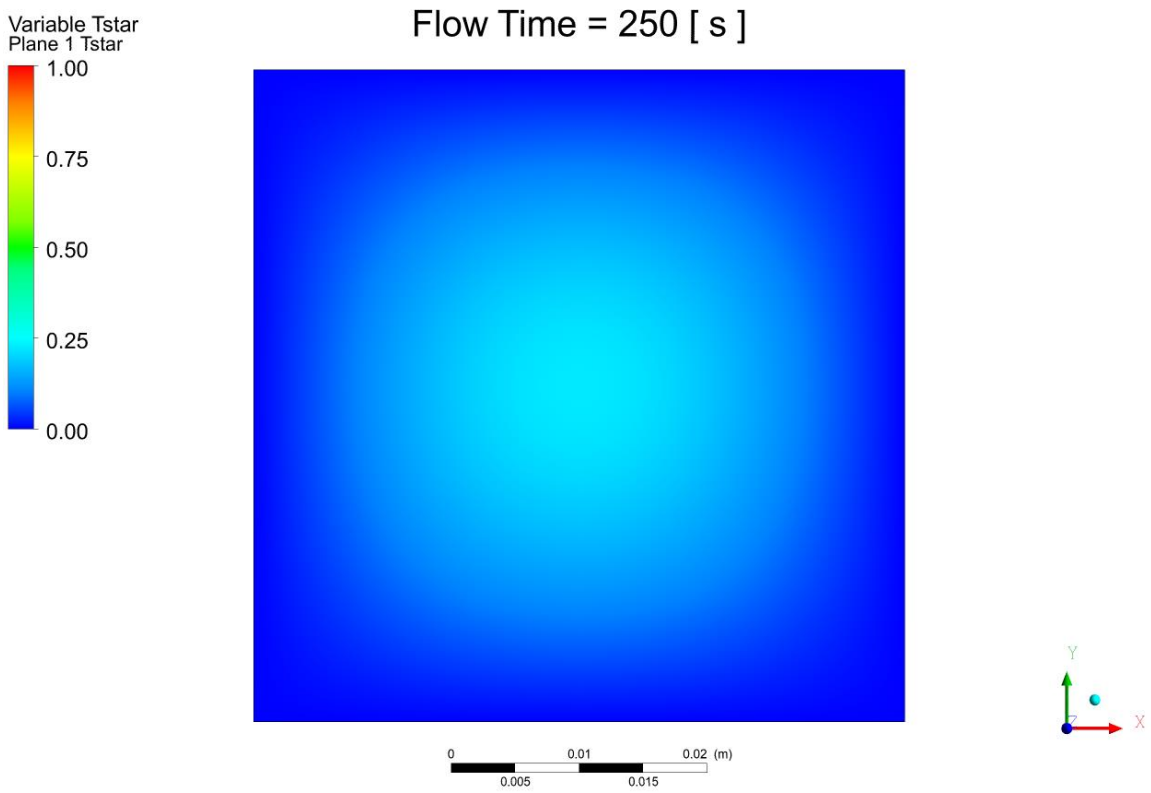

Figure 3-16. Discharge cycle dimensionless temperature at 250 seconds.

3.2 Flow Patterns

The charge cycle has flow patterns that are noteworthy, as the recirculation patterns reveal why melting occurs at the corners. The streamline plot of Figure 3-17 shows recirculation zones at the corners of the interior fluid domain. These recirculation zones appear to be responsible for the accelerated melting at these regions compared to regions closer to the midpoints of each wall. Other studies have also observed similar flow behavior in simulations on molten chloride salts in OpenFOAM [24] compared to simulations performed for this research on ANSYS Fluent. The vector plot of Figure 3-18 is also useful for determining the direction of these recirculation zones. Near the upper

corners, the vectors nearest the solid phase are pointing downward, which is causing some melting to occur by forcing higher temperature fluid across the mushy zone.

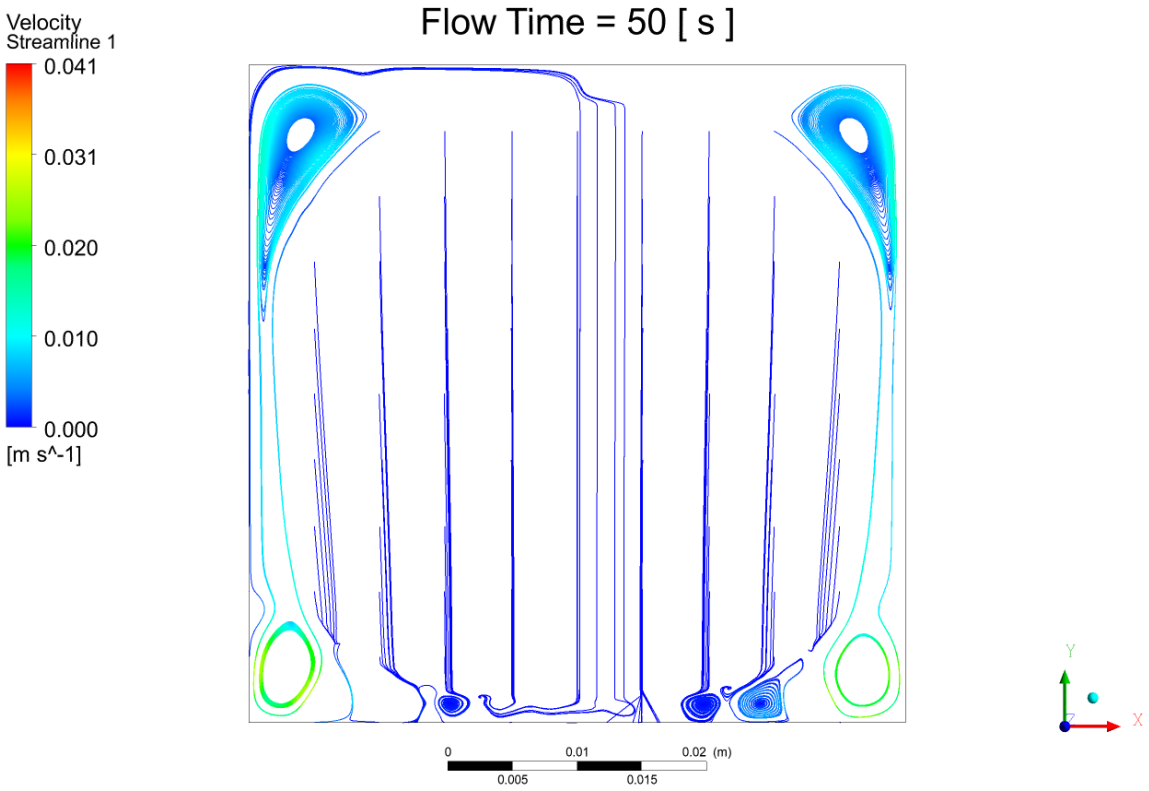

Figure 3-17. Streamlines plot of charge cycle at 50 seconds.

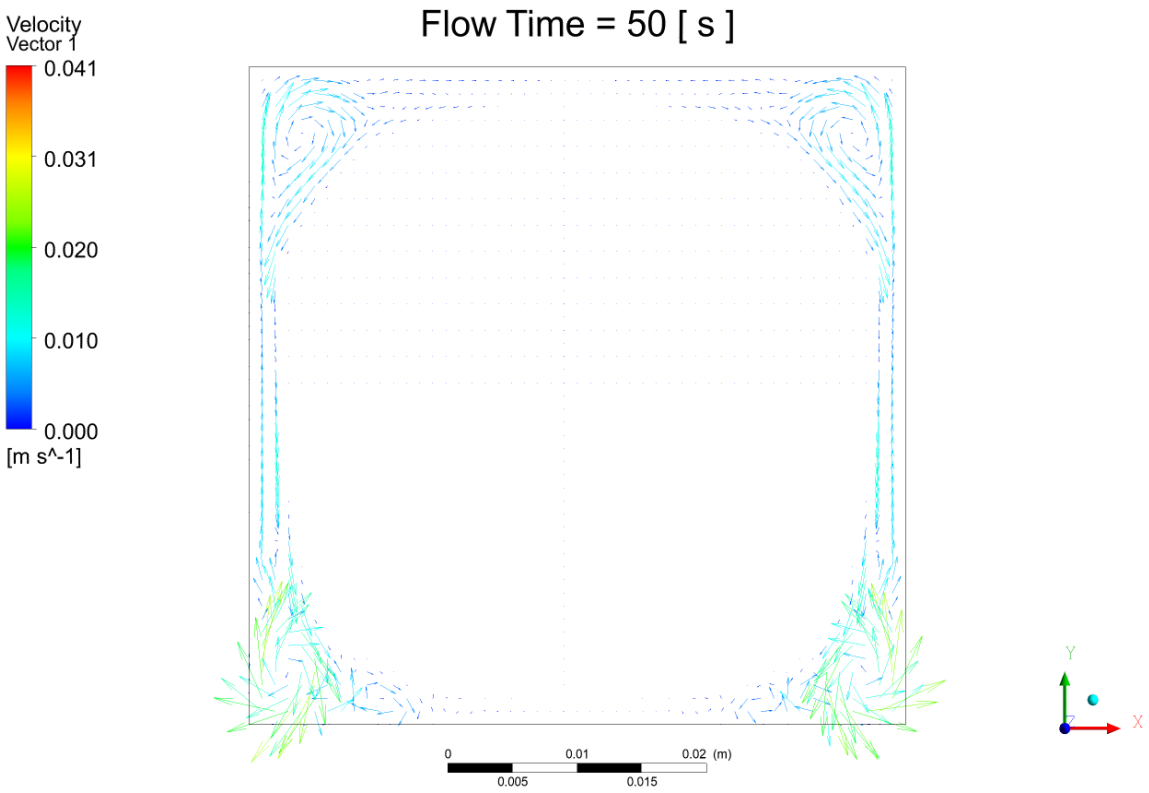

Figure 3-18. Vector plot of charge cycle at 50 seconds.

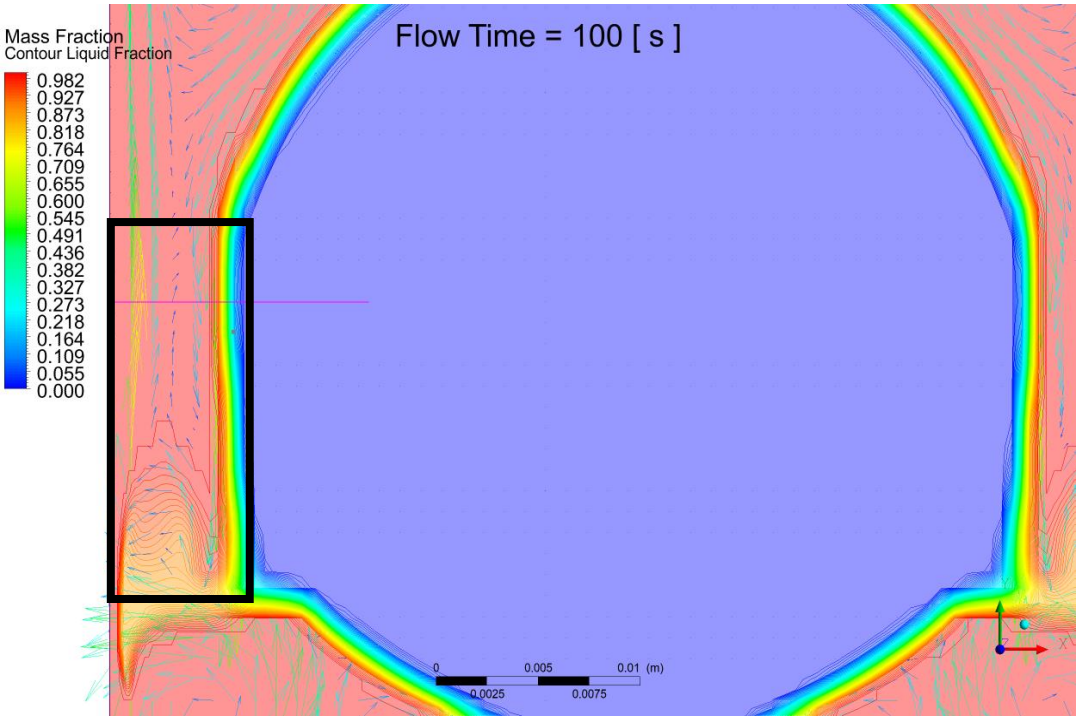

Figure 3-19. Velocity vector superimposed over a liquid fraction contour, at 100 sec.

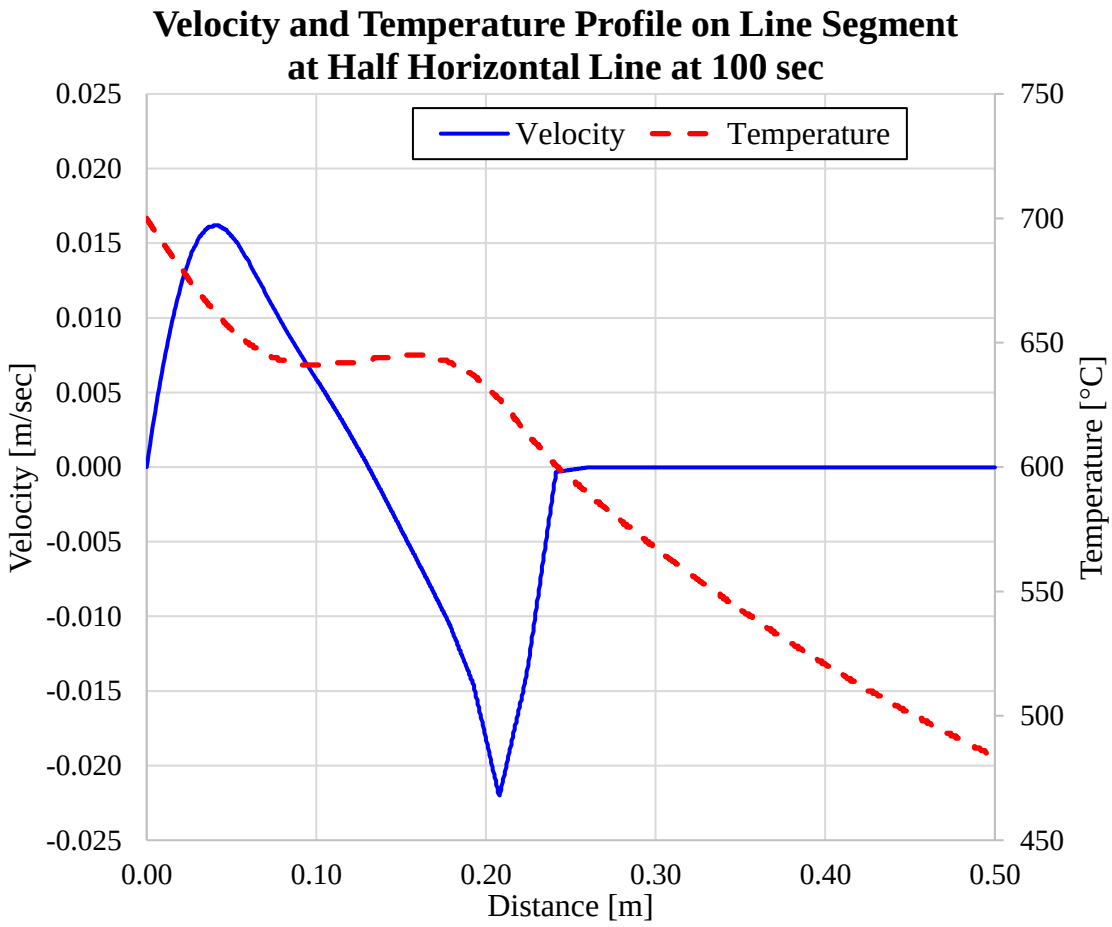

Figure 3-20. Velocity and temperature profile on a line segment at time 100 sec.

The superimposing of different plot types allows for understanding how the flow behaves and can validate Fluent setup assumptions. The contour plot of Figure 3-19 shows velocity vectors over the liquid fraction contour plot. The vectors are only present in regions where the liquid fraction is above 0, and particularly well represented in regions with liquid fraction of 1. Figure 3-19 was particularly useful for confirming that the Rayleigh number calculated would assume laminar flow. The black boxed region is approximately 0.006m in width and 0.02m in height. In this region, the Rayleigh number was calculated as 2.51×10^6, which means it is well below the transition into turbulent

flow. Since this boxed region had a Rayleigh number greater than 1,708 the buoyancy force overcame the viscous forces and therefore the threshold for buoyancy driven flow.

The chart in Figure 3-20, showing velocity and temperature profile on a line segment, is typical of rectangular enclosures. Natural convection of rectangular enclosures with different temperature side walls produces this kind of profile where velocity of fluid near the hot wall moves up against gravity, and the velocity near the cold wall moves downward with gravity. This velocity profile implies that there is a region somewhere in the middle where the flow is zero. The temperature profile also resembles that of solving temperature profiles for rectangular enclosures of constant, unequal wall temperatures. The end of the mushy zone can be considered a wall of constant cold temperature, as that boundary is a constant liquidus temperature.

3.3 Curves of Temperature, Liquid Fraction, Heat Transfer

The quantitative results of the charge and discharge simulations provide useful insight into the average condition throughout the duration of the simulations. The mass average temperature curves in Figure 3-21 shows how hot is the ROC in the TES. The mass average liquid fraction in Figure 3-22 shows how much of the bulk ROC becomes liquid in charge cycle and how much liquid remains in the discharge cycle. This chart becomes a useful insight into the Nusselt number analysis later in this discussion. The area weighted heat flux in Figure 3-23 shows the progression of the heat transfer throughout the duration of the charge and discharge cycles.

The charge cycle has a change in behavior of the temperature and heat flux once the system has achieved 100% phase change from solid to liquid. At about 122 seconds the

entire flow domain is liquid and temperature and heat flux change behavior. The temperature chart in Figure 3-21 shows a slight acceleration in change in temperature at 122 seconds. This behavior has been seen in other studies [25] [26] [27] [28].

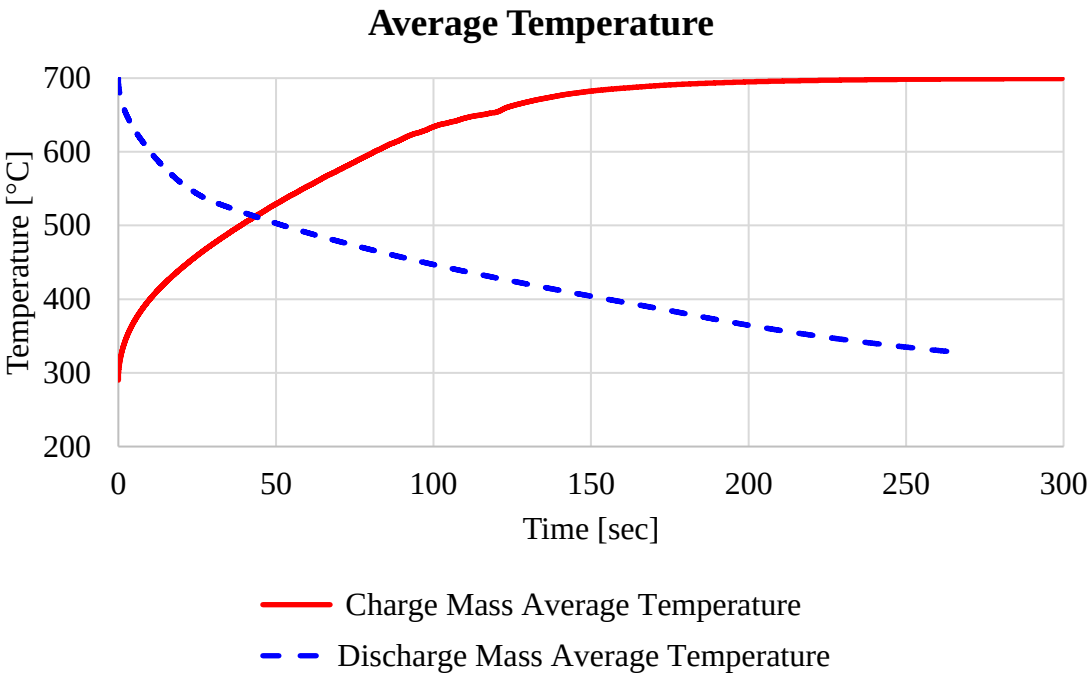

Figure 3-21. Mass average temperature over the duration of the simulation.

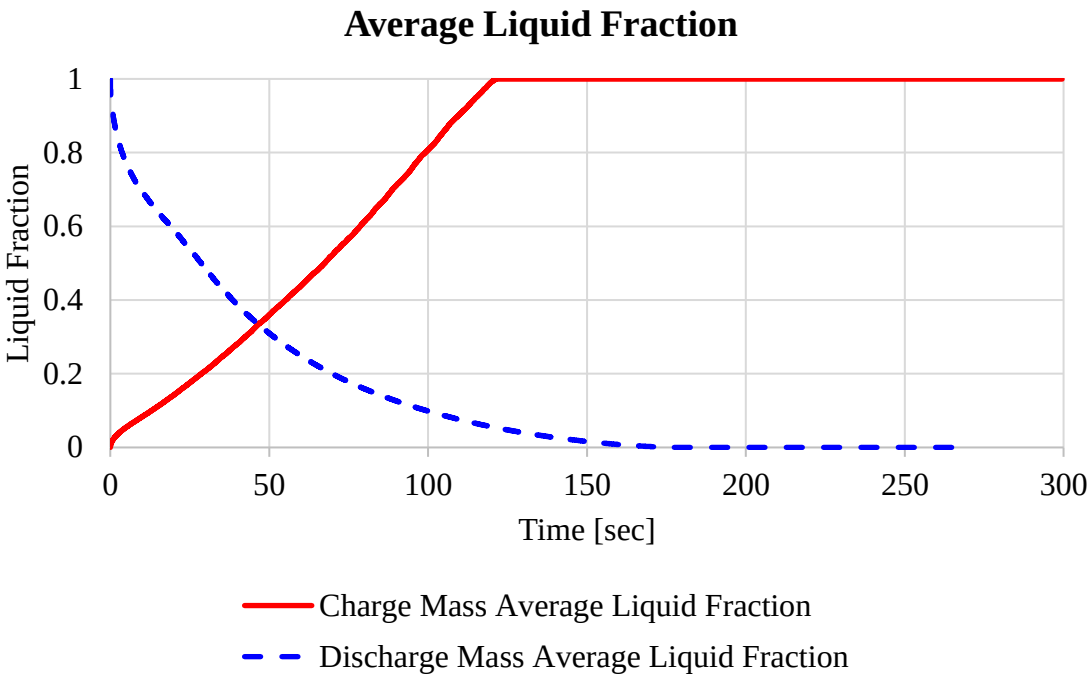

Figure 3-22. Mass average liquid fraction over the duration of the simulation.

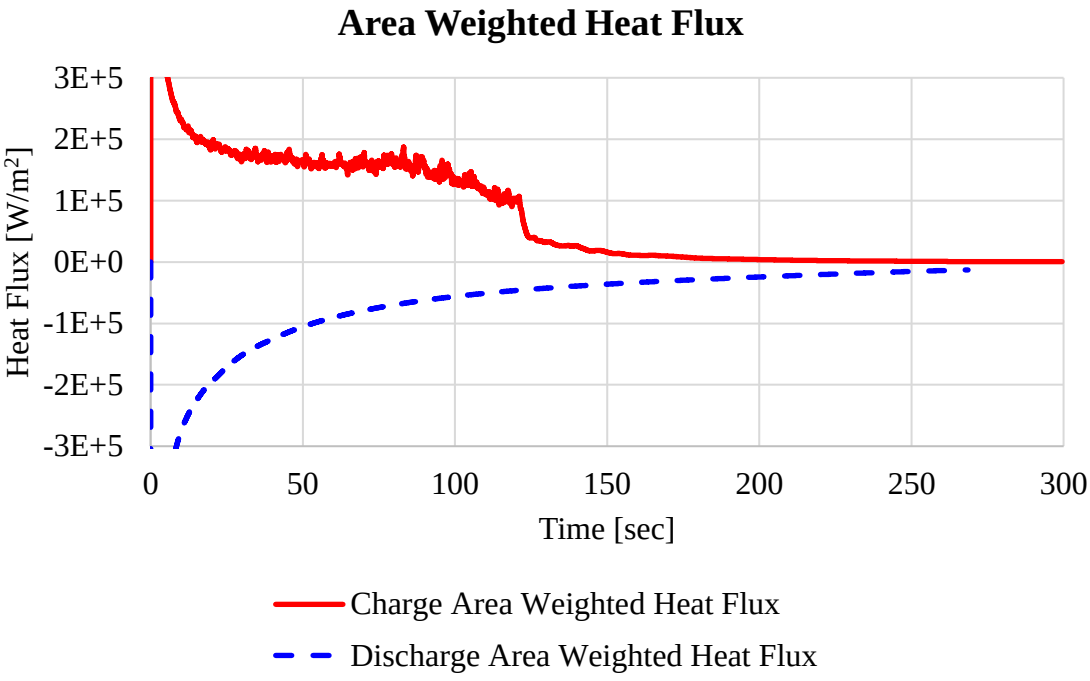

Figure 3-23. Area weighted heat flux over the duration of the simulation.

3.4 Nusselt and Fourier Number Analysis

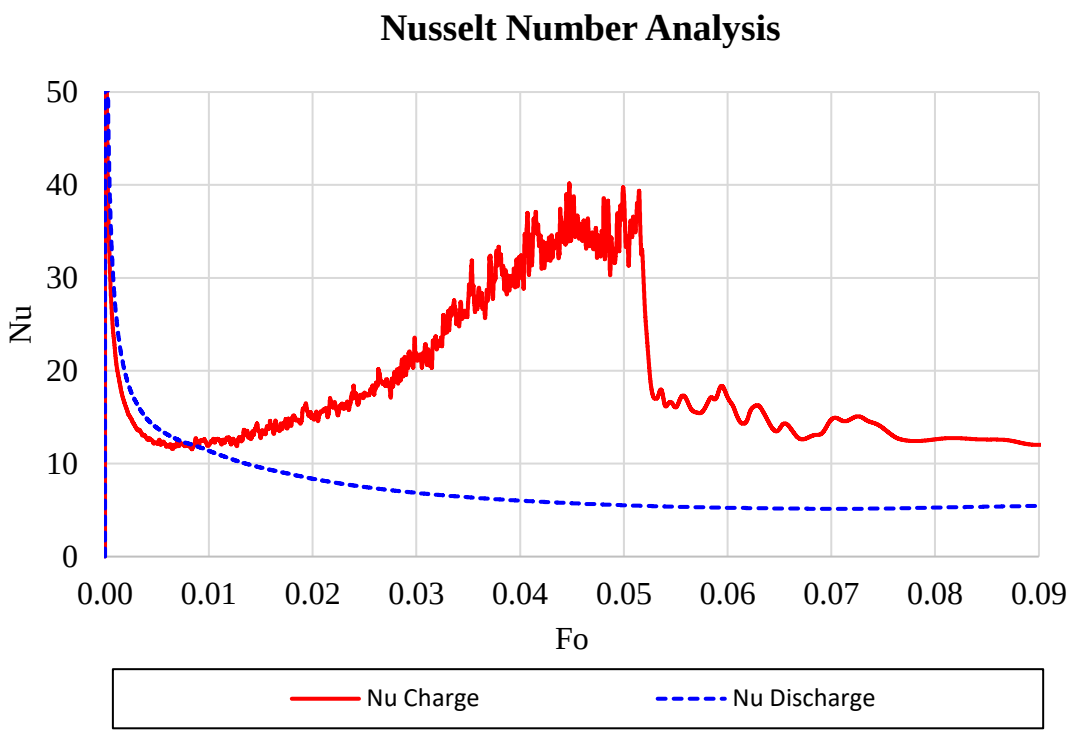

Figure 3-24. Nusselt number vs Fourier number for charge and discharge.

Nusselt number analysis is required to determine whether the heat transfer mechanism is dominantly convective or conductive. The Nusselt number describes the ratio at which the heat transfer is convective over conductive, which is commonly determined in convection heat transfer problems. The Nusselt number was derived by the area weighted average heat flux calculated by Fluent. First the heat flux, q" , was manually converted into convection heat transfer coefficient, $h_{conv} = q''/(T_w - T_{average})$, before being converted into Nusselt number by $Nu \equiv hL/k$. Figure 3-24 shows that the charge cycle has a comparatively larger Nusselt number than the discharge cycle because the fluid motion is driven by heated walls that have a high temperature gradient. The discharge cycle produces solid ROC along the side walls which insulates the remaining liquid ROC.

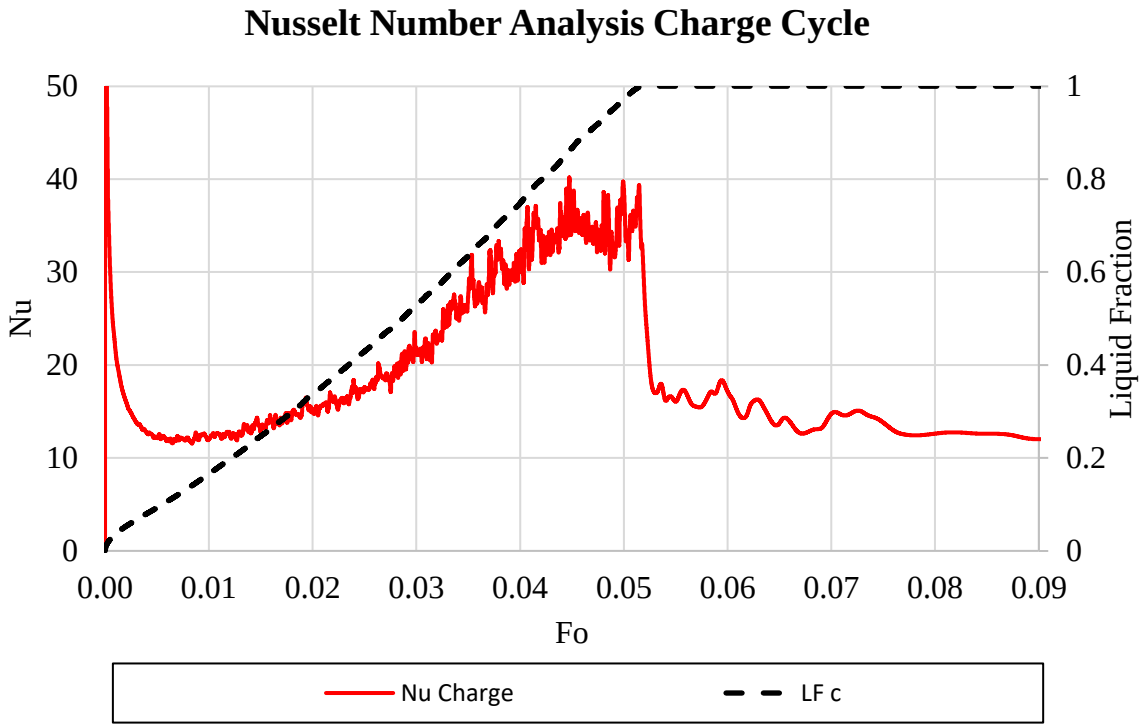

Figure 3-25. Charge cycle Nusselt no. and Liquid fraction vs. Fourier no.

When analyzing the Nusselt number for just the charge cycle, it is helpful to superimpose it over the liquid fraction to explain the peak. The graph on Figure 3-25 shows that the Nusselt number increases as the ratio of liquid increases. Once all of the initially solid ROC becomes a liquid the Nusselt number begins to decrease as the temperature of the liquid quickly reaches thermal equilibrium with the constant temperature walls. When performing the same analysis of Nusselt number and liquid fraction for the discharge cycle the observed trend is that both values decrease monotonically to an asymptote of zero. Figure 3-26 shows this behavior for the discharge cycle of Nusselt number and liquid fraction versus the Fourier number. The Fourier number was calculated as , $Fo = \alpha t/L^2$, where t is the flow time and L is the characteristic length scale of 2 inches.

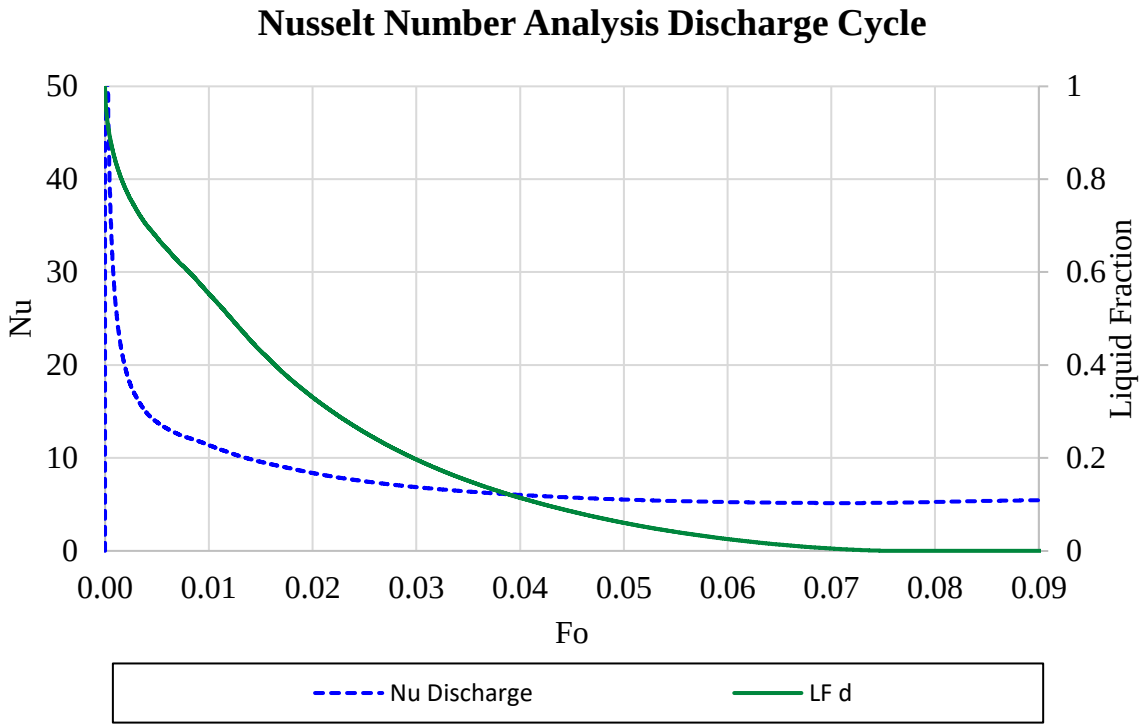

Figure 3-26. Discharge cycle Nusselt no. and Liquid fraction vs. Fourier no.

Analyzing the dimensionless temperature in accordance with Eq 11 allows for performance comparison between different TES simulations and for different temperature ranges. This data will inform the TES device designer how to space apart the HTF delivery tubes throughout the ROC. The diagram in Figure 3-40 shows a typical design consideration for how far apart tubes have to be in order to optimize heat transfer. Keeping many tubes together will increase the rate of heat transfer, but at the cost of adding more tubes. Adding too many tubes will also displace the volume of ROC that can be added, decreasing the total amount of stored thermal energy. These are some of the design considerations that are made by looking at the simulated effects of different size containers.

3.5 Comparing Constant vs Temperature Dependent Properties

Since it was previously mentioned that constant properties were tested to make a working melting and solidification model [22] it is then useful to make comparisons. The 2x2 inch geometry and 100x100 grids were simulated with only the properties being different. The following charts show the quantitative differences between simulating using constant properties from Table 2-3 and temperature dependent and weighted average properties. The label "CT" represents the constant properties and the "TD" label represents the temperature dependent and weighted average properties. The "C" label represents charge cycle and "D" represents discharge cycle.

The primary takeaway from comparing between these two properties is that the temperature dependent property ROC melted and solidified sooner than the constant property ROC. The liquid fraction chart for charge in Figure 3-27 shows that the temperature dependent property melted fully in just 120 seconds whereas it took the constant property about 460 seconds. The cause of this has significant affect by the latent heat of fusion. The constant properties from Table 2-3 shows a latent heat of fusion of 520,000 [J/kg] whereas the calculated weighted average properties is 314,116 [J/kg] from Table 2-2. The temperature dependent properties also has a lower starting heat capacity in Figure 2-8, so the material also had less capacity to store heat.

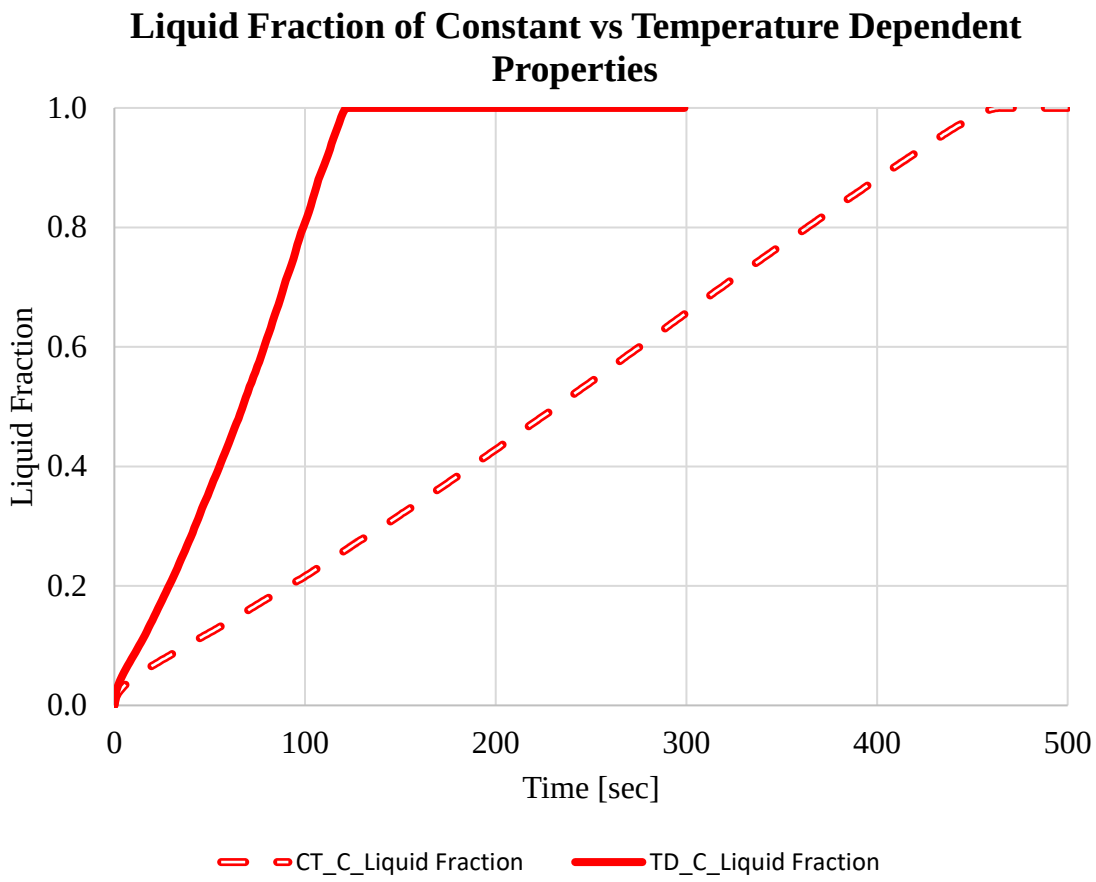

Figure 3-27. Comparison of liquid fractions of charge cycle.

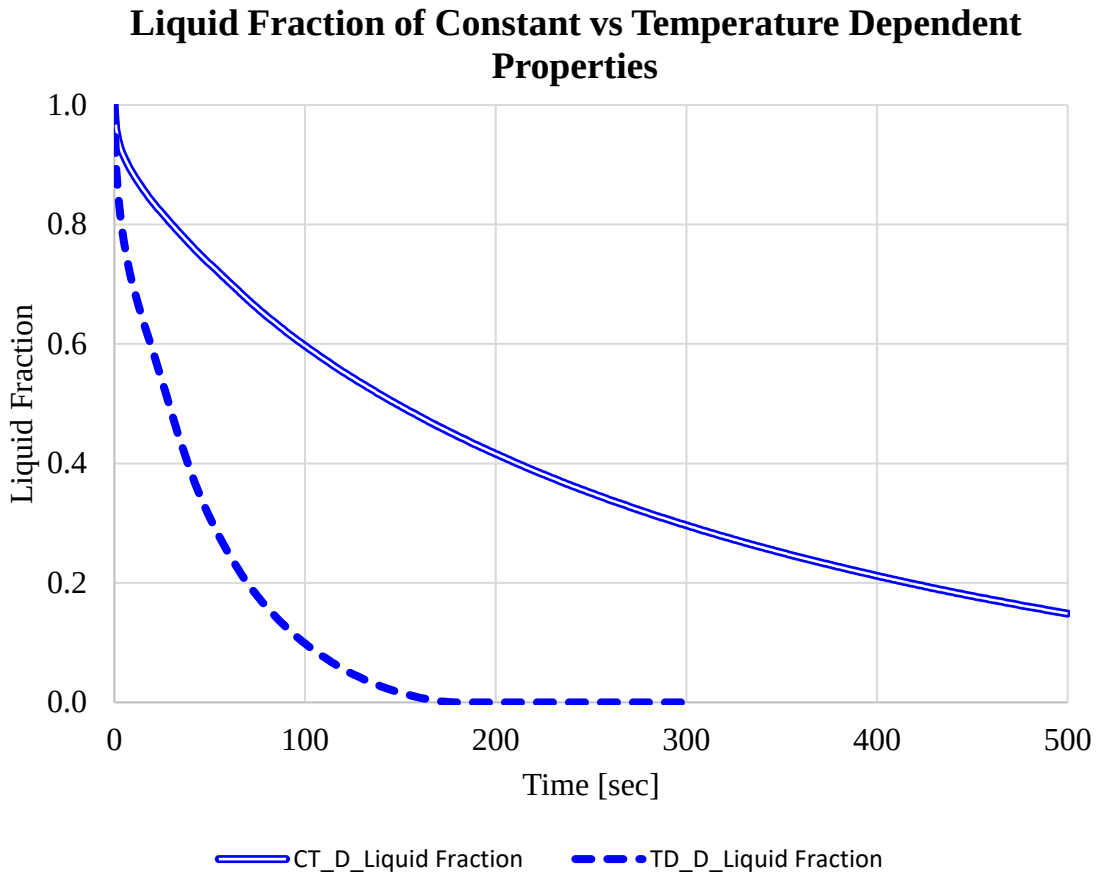

Figure 3-28. Comparison of liquid fraction of discharge cycle.

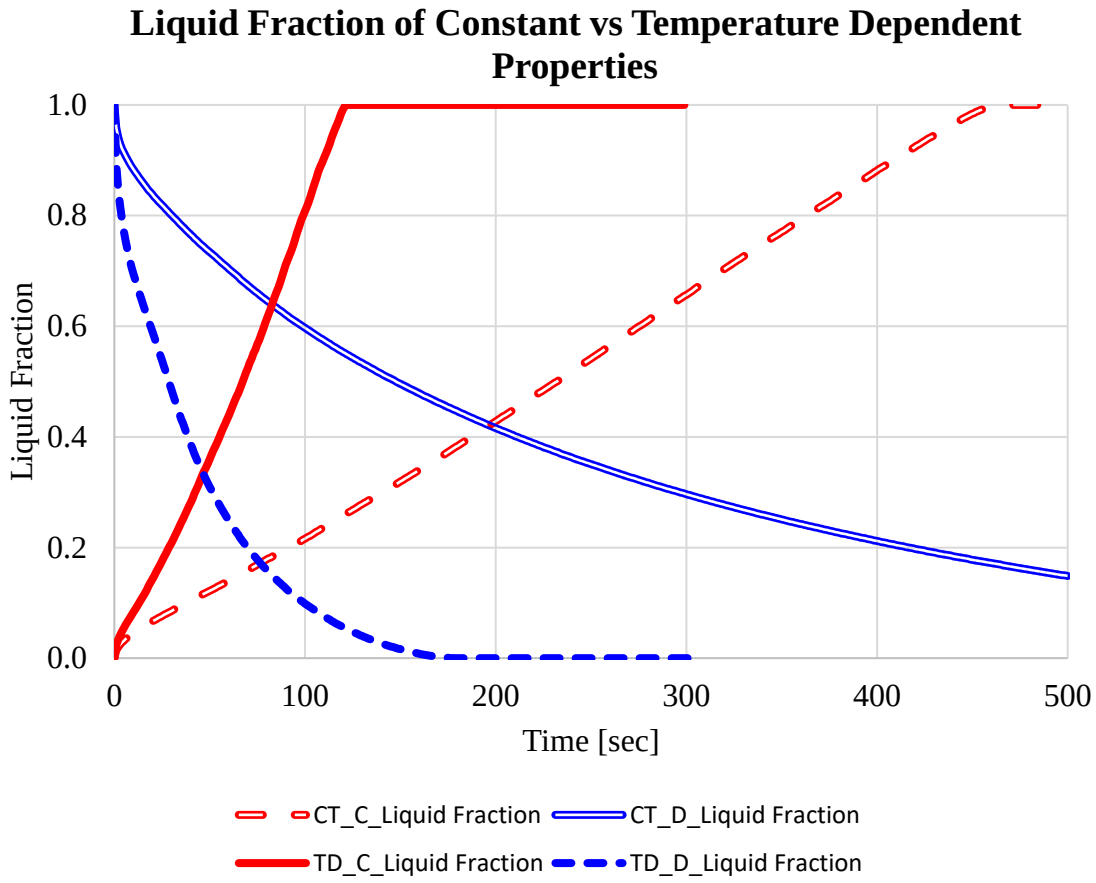

Figure 3-29. Comparison of liquid fraction, summary of charge and discharge cycles.

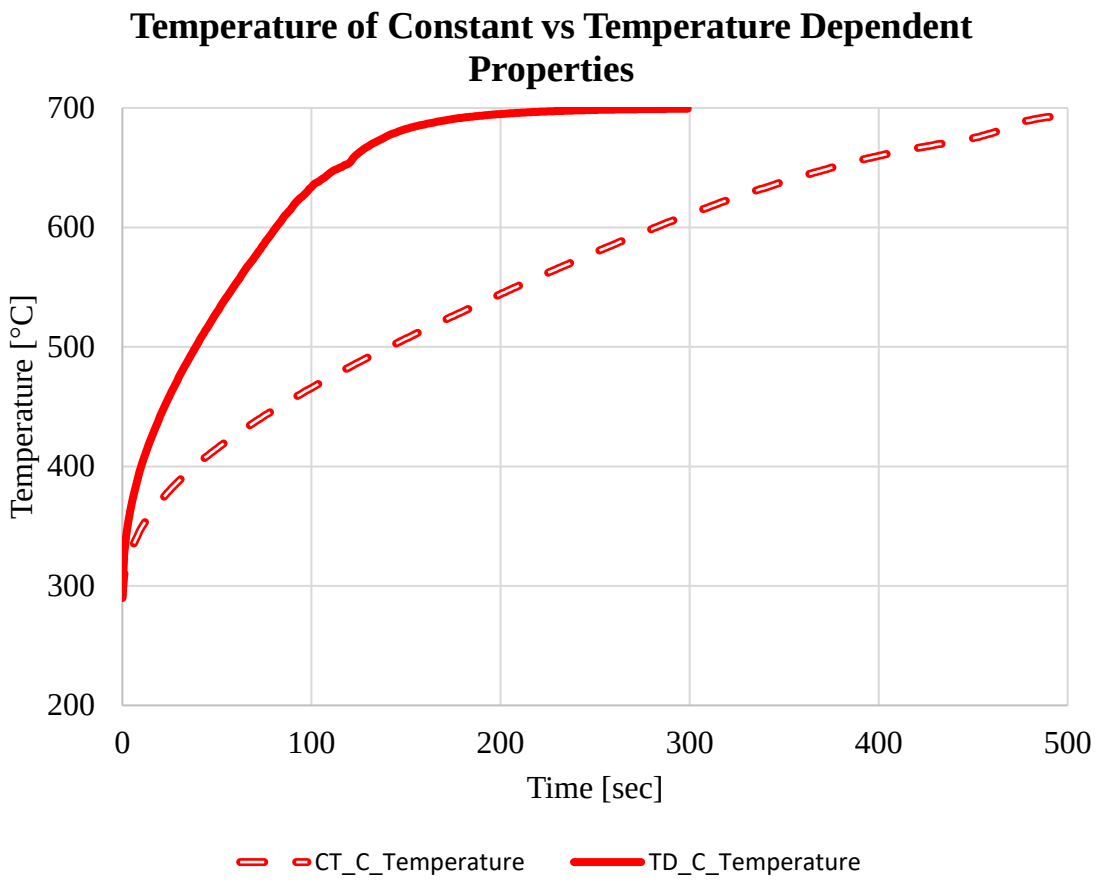

Figure 3-30. Comparison of temperature of charge cycle.

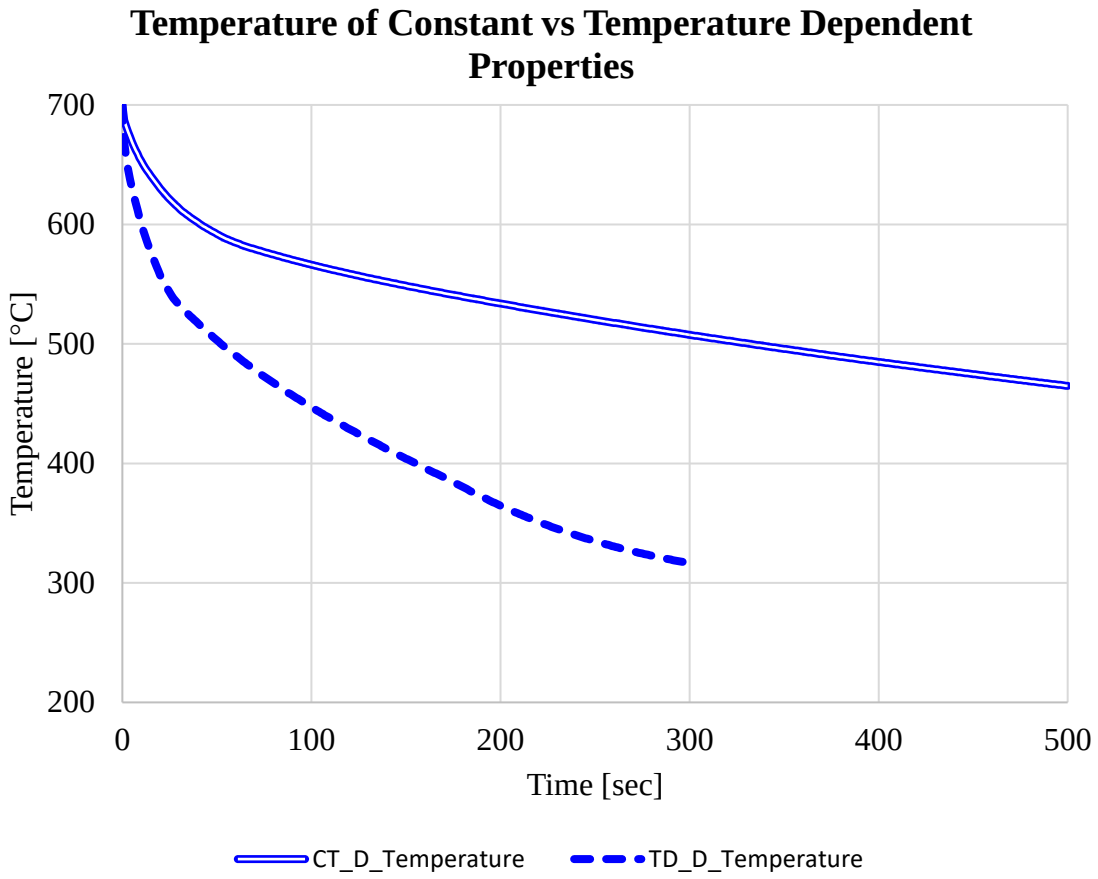

Figure 3-31. Comparison of temperature of discharge cycle.

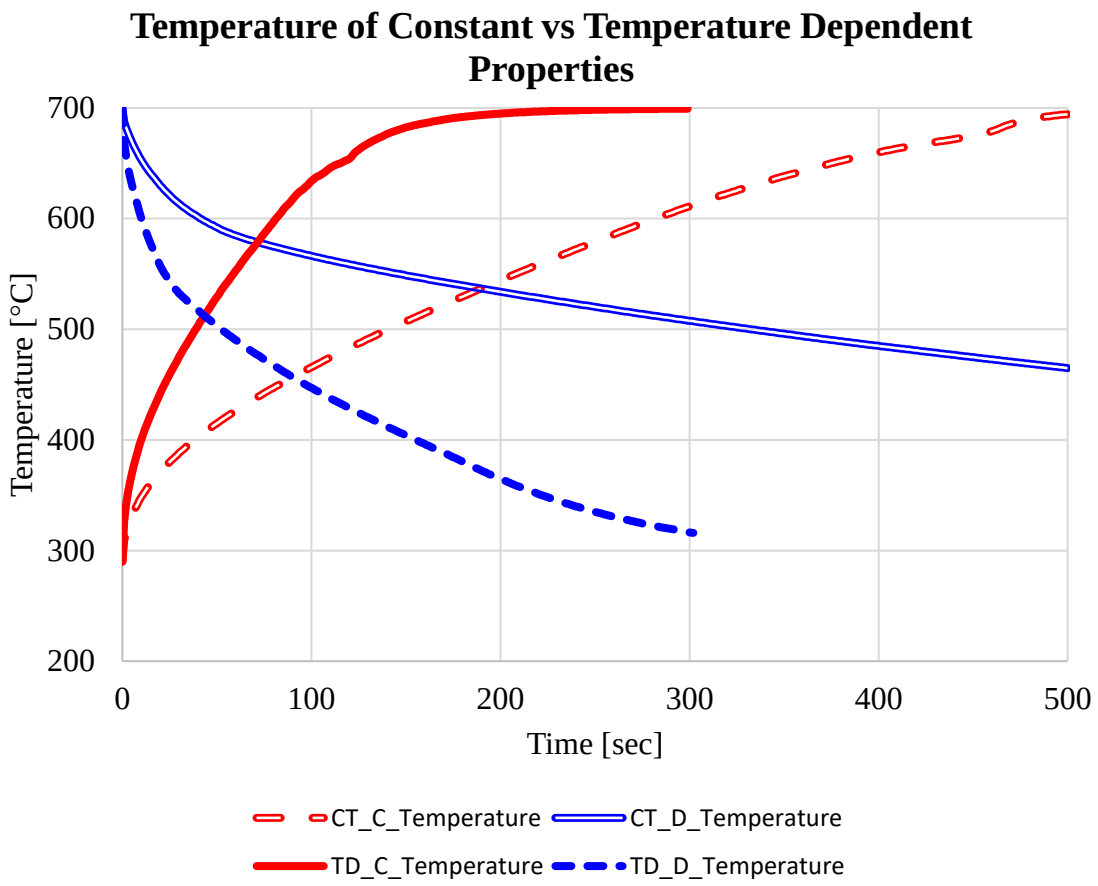

Figure 3-32. Comparison of temperature, summary of charge and discharge cycles.

The comparison of the heat fluxes helps to reveal how much heat is transferred during each cycle. The estimated integration of tabulated results is listed in Table 3-1, where the units are [J/m^2] because of multiplying the heat flux [W/m^2] by the time in [sec]. The main takeaway from this is that the amount of energy stored and extracted is higher for temperature dependent, weighted averaged properties of ROC.

Table 3-1. Energy flux for each scenario measured in [J/m^2]

Constant Charge	Constant Discharge	Temperature Dependent Charge	Temperature Dependent Discharge
1.78E+07	-1.29E+07	2.25E+07	-2.01E+07

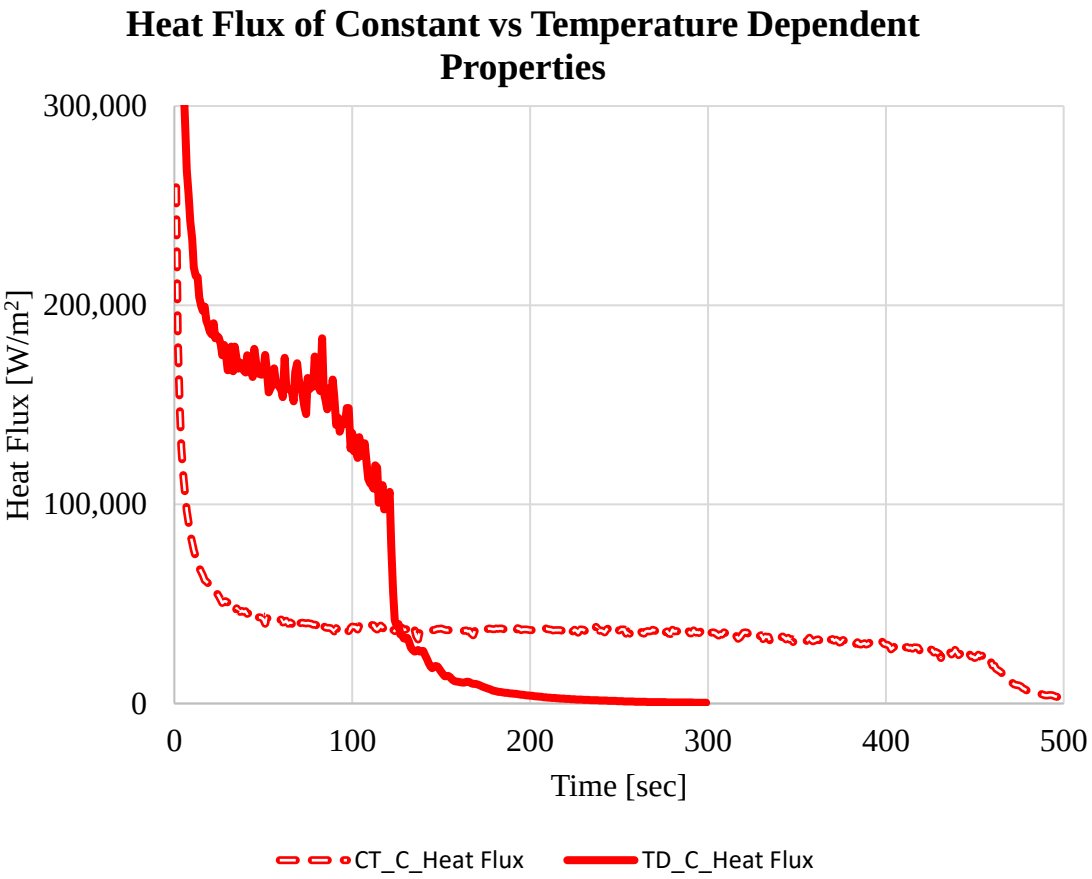

Figure 3-33. Comparison of heat flux of charge cycle.

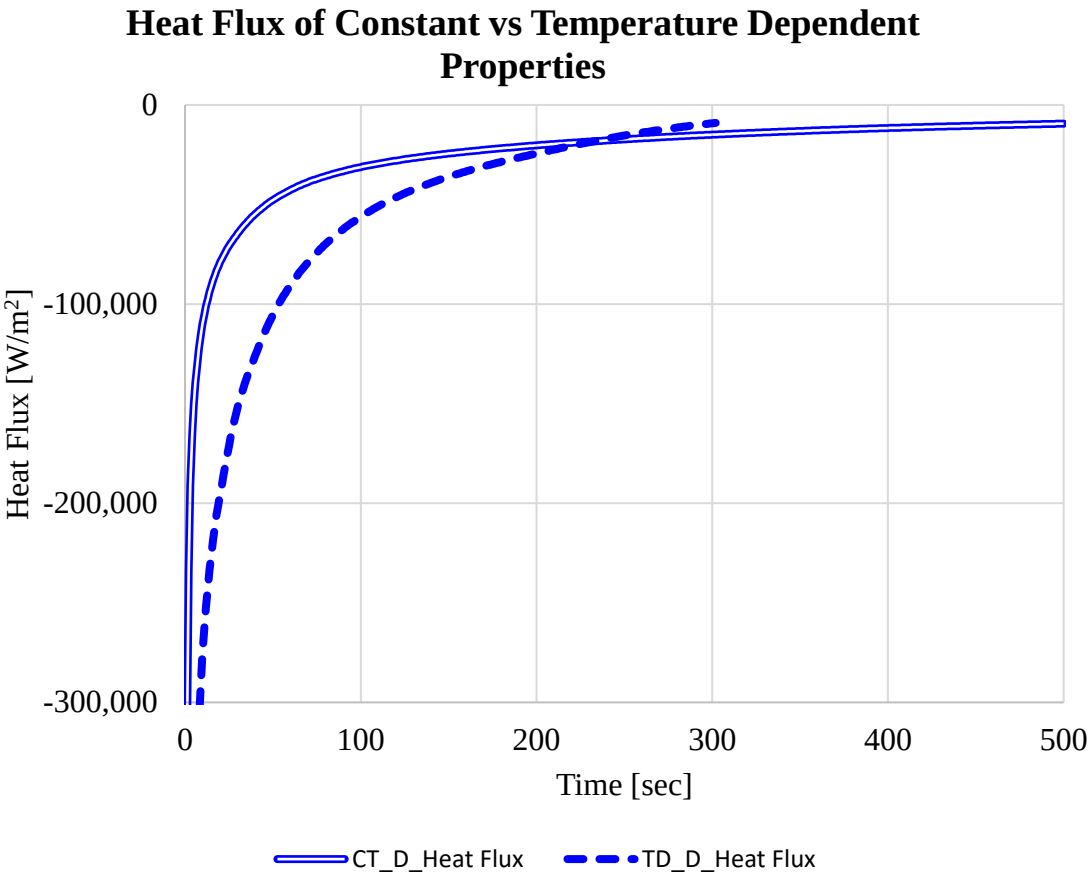

Figure 3-34. Comparison of heat flux of discharge cycle.

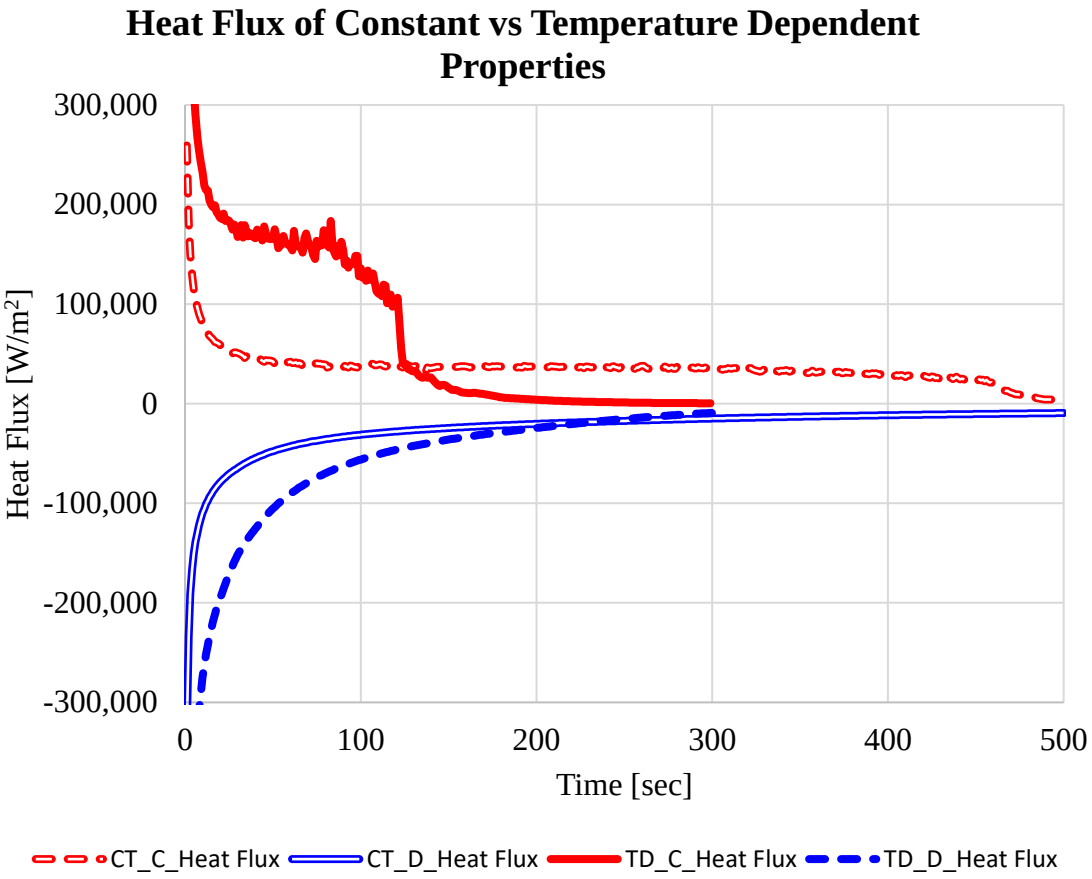

Figure 3-35. Comparison of heat flux, summary of charge and discharge cycles.

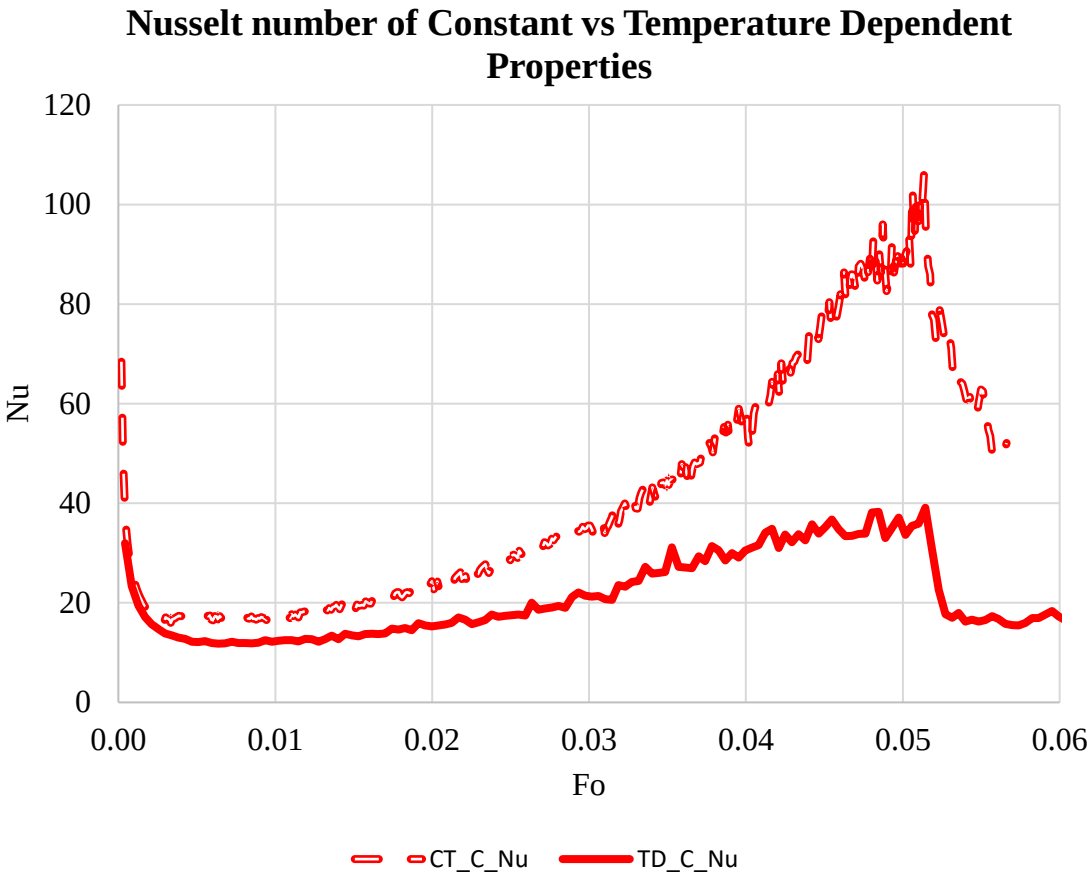

Figure 3-36. Comparison of Nusselt number of charge cycle.

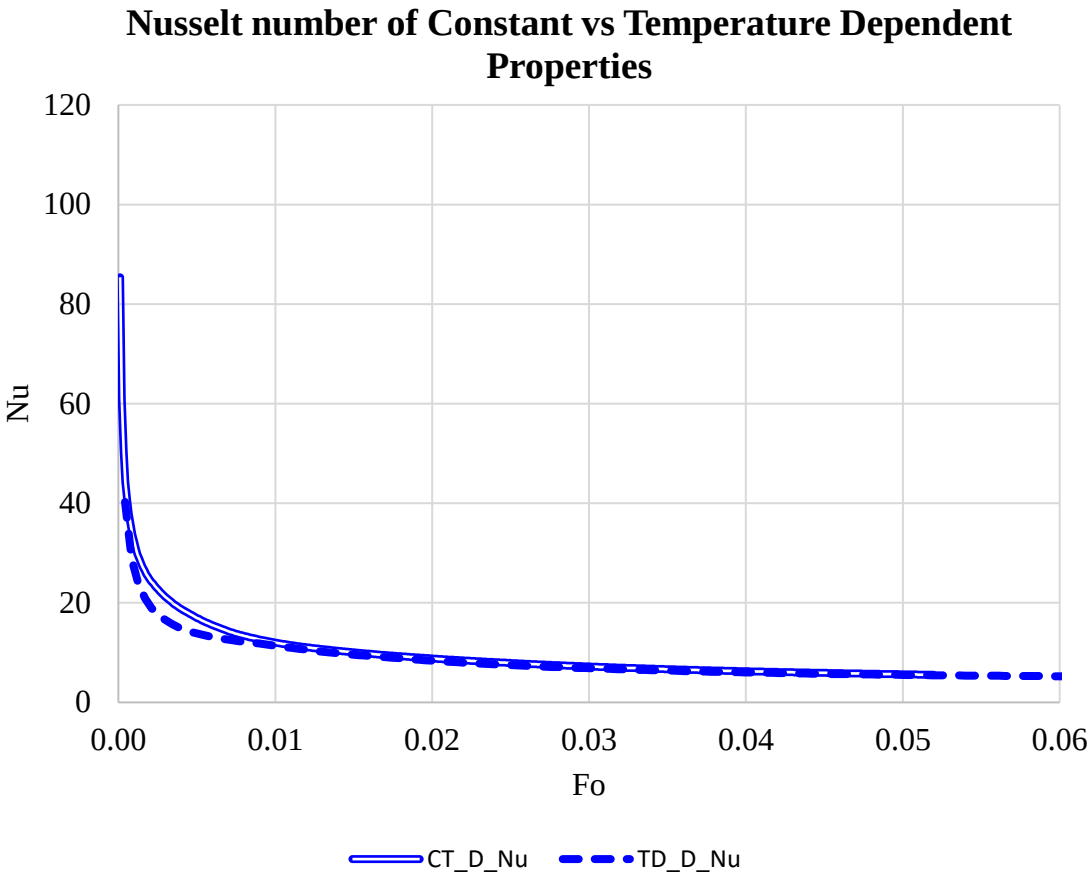

Figure 3-37. Comparison of Nusselt number of discharge cycle.

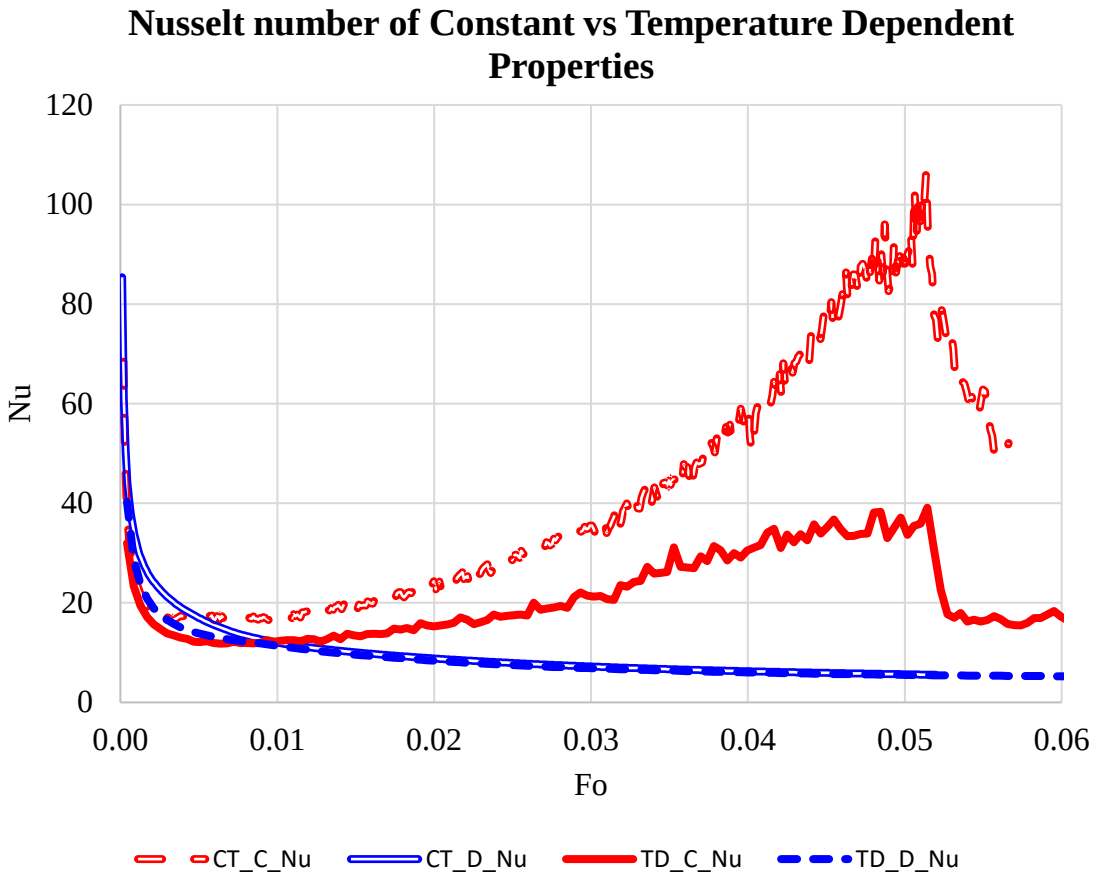

Figure 3-38. Comparison of Nusselt number, summary of charge and discharge cycles.

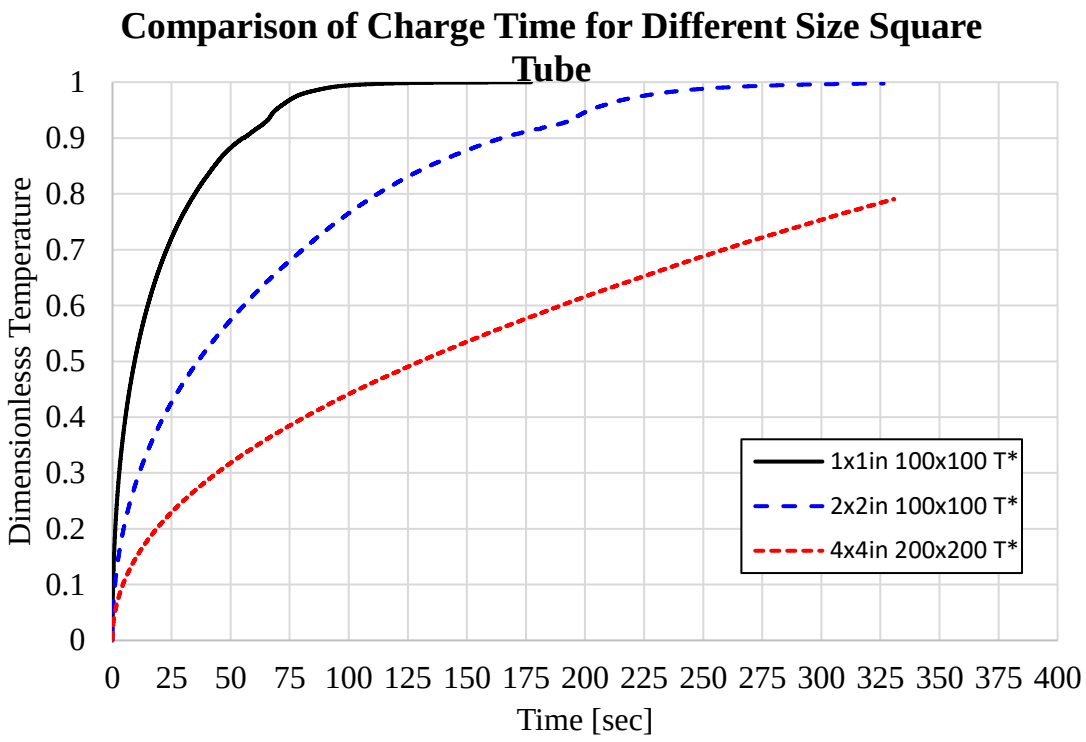

Figure 3-39. Comparison of dimensionless temperature for different sized tubes.

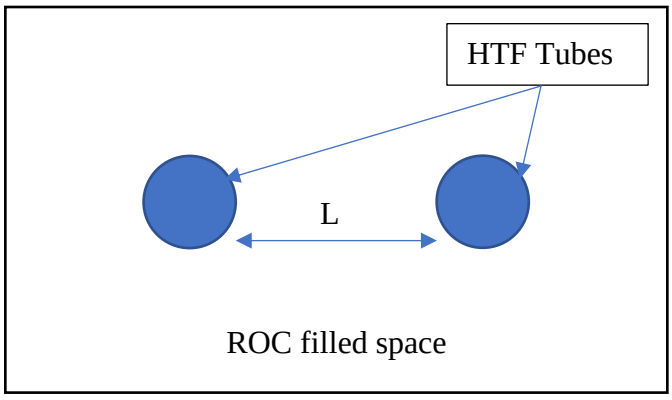

Figure 3-40. Cross section of TES showing HTF tube through ROC filled space.

When considering how to design a TES device it is important have optimal spacing of surfaces that make contact with the PCM. One can design a set of parallel running tubes in a larger container of a PCM filled cavity and space each tube apart a certain distance, illustrated by Figure 3-40. Determining the length, *L*, requires designing how long the cycles should last. By simulating the square tubes of different side lengths, the duration can be determined and used as a design parameter. The results of simulating different square tube lengths are in Figure 3-39 showing that the smaller distance will result in faster cycle times, and further spaced apart walls have a much longer time to finish a cycle. The chart in Figure 3-39 used dimensionless temperature to show that the rate at which a TES device achieves full charge from 0.1 to 0.9 is able to be represented for any set range of process temperature.

The hope of studying further spaced apart tubes is that the cost of a TES unit can be lowered by installing fewer tubes to deliver HTF. Also, a TES device that had too many tubes would sacrifice on total stored amount of energy. Material costs need to be low in order for an adoption of this technology to launch successfully. Saving on HTF tubes is the first step towards building an affordable TES device. Any known materials resistant to chlorine salt corrosion also contributes to the cost of the device, and determining the role of corrosion by ROC is a long term investment into the survival of a fully developed TES system using ROC as the PCM.

CHAPTER 4 CONCLUSION

Development of a computational model is successful at simulating the heat transfer and phase change process of inorganic ROC salt mixture during the charge and discharge cycle of an ROC-based TES system. The model used the Voller and Swaminathan method to iteratively calculate enthalpy and the momentum and energy equations. The qualitative results show that the phase change process and buoyancy driven flows significantly impact the charge and discharge cycles. Boundary layers predicted by natural convection theory form on the left and right vertical walls and Rayleigh-Bernard convection occur on the top and bottom horizontal walls. A Nusselt number analysis determined stronger convection during the charge cycle and weaker convection during discharge cycle.

The engineering applications from this computational model can be used to develop an efficient size TES device by adjusting surface contact of the ROC-PCM and the length between walls. A particular challenge will be decreasing the discharge time in order to meet peak energy demands to the grid. Overall, this study shows that natural convection via buoyancy driven flow in a sealed container can be implemented in a TES device, hopefully as part of a larger grid storage scale of energy storage.

CHAPTER 5 FUTURE WORK

5.1 Salt Characterization

Since the current thermophysical properties of this ROC is estimated based on assumed weighted averages of the individual properties the continuation of this work will inevitably require experimental verification. There are different methods of measuring properties such as heat capacity using differential scanning calorimetry (DSC), like how the salt mixture FLiNaK was measured in [29]. Measuring viscosity would require a specialized rheometer that has an electric heater and a specialized cup and bob made of an Inconel alloy that can run up cost of experiment. The challenge, beyond budget concerns, is that the ROC substances are mixtures that come from any part of the world and some could be nonuniform. This poses the challenge that the TES device must be capable of accommodating all or many types of ROC based on the average composition. A ROC sample with more NaCl will behave differently than one with more CaCO3, and any combination of the primary components. Since the motivation behind this technology is to use the ROC as is with minimal processing and no separation, it will be important to fully understand the properties of the mixture.

5.2 Design

Once the ROC properties are known, for even just one of consistent composition, a design of a TES device will have to be optimized for its heat transferability. The faster the heat can disperse throughout the bulk the more efficient the device can function as a heat battery. Since the ROC acts like an insulator when solid, one possible addition to the

design would be to include fins to increase the surface area of heat extracted from the ROC.

5.3 Corrosion Resistance

Any material that is exposed to salt is going to need to be corrosion resistant. Since the TES device functions similarly like a heat exchanger, it must be constructed of a material that is conductive, ductile, and strong. Judith Gomez at NREL [30] tested candidate metal alloys have been tested for corrosion resistance in molten chloride salt environments. Some of the alloys Judith tested were stainless steels of known high corrosion resistance and other nickel superalloys that were specifically engineered for corrosion resistance. The testing of materials resistant to corrosion and selection of the material that is both cost effective and corrosion resistant will be an important design choice for the longevity of any constructed TES device.

REFERENCES

[1] M. Majumder, "Impact of Urbanization on Water Shortage in Face of Climatic Aberrations," *Springer,* 2015.

[2] P. &. J. I. Palomar, "Impacts of Brine Discharge on the Marine Environment. Modelling as a Predictive Tool," *Desalination, Trends and Technologies*, 2011.

[3] "U.S. energy facts explained," [Online]. Available: https://www.eia.gov/energyexplained/us-energy-facts/.

[4] B. Jones-Albertus, "Confronting the Duck Curve: How to Address Over-Generation of Solar Energy," 12 October 2017. [Online]. Available: https://www.energy.gov/eere/articles/confronting-duck-curve-how-address-over-generation-solar-energy.

[5] P. D. Myers and Y. D. Goswami, "Thermal Energy Storage Using Chloride Salts and Their Eutectics," *Applied Thermal Engineering*, vol. 109, pp. 889-900, 25 October 2016.

[6] R. G. Reddy, "Novel Molten Salts Thermal Energy Storage for Concentrating Solar Power Generation," Tuscaloosa, Alabama, 2013.

[7] N. Calvet, A. H. Slocum, A. Gil, B. Grange, R. Lahlou, T. T. Hamer, M. Diago, M. Tetreault-Friend, D. S. Codd, D. L. Trumper and P. R. Armstrong, "Dispatchable solar power using molten salt directly irradiated from above," *Solar Energy,* vol. 220, pp. 217-229, 15 May 2021.

[8] P. Zhang, F. Ma and X. Xiao, Thermal energy storage and retrieval characteristics of a molten-salt latent heat thermal energy storage system, vol. 173, Shanghai: Applied Energy, 2016, pp. 255-271.

[9] D. Kearney, B. Kelly, R. Cable, N. Potrovitza, U. Herrmann, P. Nava, R. Mahoney, J. Pacheco, D. Blake and H. Price, "Overview on use of a Molten Salt HTF in a Trough Solar Field," in *NREL TES Workshop*, Golden, 2003.

[10] G. J. Janz, "Thermodynamic and transport properties for molten salts: correlation equations for critically evaluated density, surface tension, electrical conductance, and viscosity data," *American Chemical Society and the American Institute of Physics for the National Bureau of Standards*, vol. 17, 1988.

[11] R. N. Nalbandian, K. U. Girgis, B. T. Kong, U. Aguirre, A. G. Victorio, J. A. Lee and R. B. Lakeh, "Simulation of an ROC-Based thermal energy storage system in

charge and discharge cycles," in *ASME 2021 15th International Conference on Energy Sustainability,* 2021.

[12] U. Pelay, L. Luo, Y. Fan, D. Stitou and M. Rood, "Thermal energy storage systems for concentrated solar power plants," *Renewable and Sustainable Energy Reviews,* vol. 79, pp. 82-100, 2017.

[13] F. Rabah, "Lecture 3: Water Softening, Water Treatment Technology," in *Lecture presented in ENGC,* 2020.

[14] ANSYS, Inc., "ANSYS Fluent Theory Guide (16.1 ed.)," 2015.

[15] C. Arkar and S. Medved, "Influence of accuracy of thermal property data of a phase change material on the result of a numerical model of a packed bed latent heat storage with spheres," *Thermochimica Acta,* vol. 438, no. 1-2, pp. 192-201, 2005.

[16] A. Felix Regin, S. C. Solanki and J. S. Saini, "An analysis of a packed bed latent heat thermal energy storage system using PCM capsules: Numerical investigation," *Renewable Energy,* vol. 34, no. 7, pp. 1765-1773, 2009.

[17] V. R. Voller, A. D. Brent and K. J. Reid, "A Computational Modeling Framework for the Analysis of Metallurgical Solidification Process and Phenomena," *Conference for Solidification Processing,* 1987.

[18] V. R. Voller and C. Prakash, "A Fixed-Grid Numerical Modeling Methodology for Convection-Diffusion Mushy Region Phase-Change Problems," *International Journal of Heat and Mass Transfer,* vol. 30, pp. 1709-1720, 1987.

[19] V. R. Voller and C. R. Swaminathan, "Generalized Source-Based Method for Solidification Phase Change," *Numerical Heat Transfer,* vol. 19, no. 2, pp. 175-189, 1991.

[20] N. Mallya and S. Haussener, "Buoyancy-driven melting and solidification heat transfer analysis in encapsulated phase change materials," *International Journal of Heat and Mass Transfer,* vol. 164, 14 June 2020.

[21] C. Camapana, L. Cioccolanti, M. Renzi and F. Caresana, "Experimental analysis of a small-scale scroll expander for low-temperature waste heat recovery in Organic Rankine cycle," *Energy,* vol. 187, 2019.

[22] J. A. Lee, C. N. Salerno, K. U. Girgis, U. Aguirre and R. B. Lakeh, "Effect of phase change and Buoyancy-driven flows on an ROC-Based thermal energy storage system," *ASME 2021 15th International Conference on Energy Sustainability,* 2021.

[23] M. Tiberga, D. Shafer, D. Lathauwers, M. Rohde and J. L. Kloosterman, "Preliminary investigation on the melting behavior of a freeze-valve for the Molten Salt Fast Reactor," *Annals of Nuclear Energy*, vol. 132, pp. 544-554, 2019.

[24] Y. S. Jeong, S. B. Seo and I. C. Bang, "Natural convection heat transfer characteristics of molten salt with internal heat generation," vol. 129, pp. 181-192, 29 September 2017.

[25] S. Bellan, T. E. Alam, J. Gonzalez-Aguilar, M. Romero, M. M. Rahman, Y. D. Goswami and E. K. Stefanakos, "Numerical and experimental studies on heat transfer characteristics of thermal energy storage system packed with molten salt PCM capsules," *Applied Thermal Engineering*, vol. 90, pp. 970-979, 5 November 2015.

[26] S. Bellan, J. Gonzalez-Aguilar, M. Romero, M. M. Rahman, Y. D. Goswami and E. K. Stefanakos, "Numerical Investigation of PCM-based Thermal Energy Storage System," *Energy Procedia*, vol. 69, pp. 758-768, May 2015.

[27] S. Bellan, J. Gonzalez-Aguilar, M. Romero, M. M. Rahman, Y. D. Goswami, E. K. Stefanakos and D. Couling, "Numerical analysis of charging and discharging performance of a thermal energy storage system with encapsulated phase change material," *Applied Thermal Engineering*, vol. 71, no. 1, pp. 481-500, 5 October 2014.

[28] F. Fornarelli, S. M. Camporeale, B. Fortunato, M. Torresi, P. Oresta, L. Magliocchetti, A. Miliozzi and G. Santo, "CFD analysis of melting process in a shell-and-tube latent heat storage for concentrated solar power plants," *Applied Energy*, vol. 164, pp. 711-722, 15 February 2016.

[29] T. Lichtenstein, M. Rose, J. Krueger, E. Wu and M. Williamson, "Thermochemical Property Measurements of FLiNaK and FLiBe in FY 2020," *Chemical and Fuel Cycle Technologies Division*, Vols. ANL/CFCT-20/37, 17 November 2020.

[30] J. C. Gomez-Vidal and R. Tirawat, "Corrosion of alloys in a chloride molten salt (NaCl–LiCl) for solar thermal technologies," *Solar Energy Materials & Solar Cells*, vol. 157, pp. 234-244, 14 September 2015.

APPENDIX

Calculation of Grashof number and Rayleigh number.

	g, [m/sec^2]	T, [K]	ρ, [kg/m^3]	c_p, [J/kg*K]	k, [W/m*K]	μ, [kg/m-sec]
$T_{solidus}$	9.81	873.4	2503	1127	3.095	0.001030
$T_{liquidus}$	**L [m]**	896.9	2223	1136	2.699	0.001007
$T_{w,charge}$	0.0508	973.15	2214	1179	2.694	0.000998

$$\beta_{bulk} = -\frac{1}{2214[kg/m^3]}\frac{(2223-2214)[kg/m^3]}{(896.9-973.2)[K]} = 0.0000506 \approx 0.000051\ [1/K]$$

$$\upsilon_{bulk} = \frac{\mu}{\rho} = \frac{(9.98\times10^{-4}[kg/m*sec])}{(2214[kg/m^3])} = 4.507\times10^{-7}[m^2/sec]$$

$$\alpha_{bulk} = \frac{k}{\rho c_p} = \frac{2.694[W/m*K]}{(2214[kg/m^3])(1179[J/kg*K])} = 1.032\times10^{-6}[m^2/sec]$$

$$\mathrm{Pr} = \frac{\upsilon}{\alpha} = \frac{4.507\times10^{-7}}{1.032\times10^{-6}}\frac{[m^2/sec]}{[m^2/sec]} = 0.437$$

$$Gr_{L,bulk} = \frac{(9.81[m/sec^2])(5.1\times10^{-5}[1/K])(973.2-896.9)[K](0.0508[m])^3}{(4.507\times10^{-7}[m^2/sec])^2} = 2.44\times10^7$$

$$Ra_{L,bulk} = Gr_{L,bulk}Pr = (2.44\times10^7)(0.437) = 1.07\times10^7$$